1

1 *Kinetics of Graphitization-Revision 2 #5733*

2

3

An experimental kinetic study on the structural evolution of natural carbonaceous material to graphite

6

7 **YOSHIHIRO NAKAMURA[1,*], TAKASHI YOSHINO[2] AND**

8 **MADHUSOODHAN SATISH-KUMAR[3]**

9

10

11

12 [1]Graduate School of Science & Technology, Niigata University, 2-8050 Ikarashi, Nishi-ku,

13 Niigata 950-2181, Japan

14 [2]Institute for Planetary Materials, Okayama University, Misasa, Tottori 682-0193, Japan

15 [3]Department of Geology, Faculty of Science, Niigata University, 2-8050 Ikarashi, Nishi-ku,

16 Niigata 950-2181, Japan

17

18

19

20

21

22

23 * Corresponding author. +81-025-262-6161; fax: +81-025-262-6197.

24 E-mail address: f14n002a@mail.cc.niigata-u.ac.jp (Y. Nakamura).

25

26

27

28

ABSTRACT

We report here new experimental kinetic data on the structural evolution of carbonaceous material (CM) to graphite during heating at various temperatures (1000 to 1450 °C) for various durations (10 min to 115 h) under a pressure of 1 GPa. Natural CMs extracted from sedimentary rocks in the Shimanto accretionary complex and the Hidaka metamorphic belt of Japan transformed in morphology and crystallinity with increasing temperature and annealing duration to become fully ordered graphite (d_{002} spacing ~ 3.36 Å). Transmission electron microscopy showed that both samples have undergone microstructural evolution from amorphous carbon to platy graphitic carbon. These changes match the evolution of the samples' X-ray diffraction (XRD) patterns and micro-Raman spectra. The time–temperature relations of crystal parameters obtained by XRD and micro-Raman spectroscopy demonstrated a sigmoidal transformation curve from an amorphous to a graphitic structure, suggesting complexity of these successive and/or concurrent chemical reactions are responsible for graphitization. To assess these complex chemical processes, we adopted three different approaches for formulating the graphitization kinetics using a power rate model, a Johnson-Mehl-Avrami (JMA) model and a superposition method. Irrespective of the models employed, the effective activation energies were estimated to lie between 259 and 339 kJ mol^{-1}, which are much lower than those reported previously for graphitization. Summarizing the previous studies and our results between 0.1 and 1000 MPa, we found that the effective activation energies systematically decrease as a function of pressure. Based on the experimental results in this study, the sigmoid functions obtained from the time–temperature relations can be extrapolated to low-temperature conditions at 1 GPa. Our kinetic model using unit-cell height c predicts that CM undergoing metamorphism for about 1

52 m.y. will begin to crystallize at ~ 410 °C, and will transform to fully ordered graphite at over

53 ~ 520 °C. Thus, natural graphitization undergoes a much faster transformation than reported in

54 previous studies at 1atm and could be explored in laboratory experiments using natural precursor

55 materials under pressure conditions and time spans that reflect natural conditions in the Earth's

56 crust.

57

58 **Key words:** *Graphitization, carbonaceous material, kinetic model, HPHT experiment*

59

60 **INTRODUCTION**

61

62 Carbonaceous material (CM) is a widespread accessory phase in sediments, and its composition

63 and structure are sensitive to change during metamorphism (Buseck and Beyssac 2014). The

64 structural evolution of CM to graphite is one of the most important thermal indicators for

65 geological regimes of low to medium metamorphic temperatures, and is widely used as a

66 geothermometer (Beyssac et al. 2002; Kouketsu et al. 2014). However, the process *sensu stricto*

67 is not a simple recrystallization that depends only on metamorphic temperature. The organic

68 precursor materials of CM in sediments have complex supramolecular structures (Oberlin et al.

69 1999; Schwab et al. 2005), and their evolutions in chemical composition, microstructure, and

70 crystallinity depend not only on thermal maturation but also on tectonic deformation, catalytic

71 effects, and fluid activity under lithostatic pressure (Luque et al. 1998). Such complex

72 transformations during the transition of organic matter to graphite make it difficult to understand

73 the natural structural evolution of CM, and proper assessments of these factors during

4

74   graphitization have been seldom achieved. Therefore, it is essential to consider a fundamental

75   kinetic model for natural graphitization under geological timescales and crustal temperatures.

76   The natural structural evolution of organic matter to CM, and then into graphite, mainly

77   comprises two prominent processes: carbonization and graphitization (Oberlin 1984). The early

78   stage of carbonization begins with softening and the release of aliphatic compounds and

79   heteroatoms with increasing temperature. After degradation of aliphatic CH groups, solid-state

80   reorganization (the formation of basic structure units, BSUs) progresses with the release of

81   non-condensable gases (e.g., CH_4 and H_2) from the aromatic CH groups (Oberlin et al. 1999).

82   The BSU is the minimum structural unit of the CM nanostructure. The aggregate is stacked in

83   two or three polyaromatic layers, and acts as a nucleus for the transformation of turbostratic to a

84   graphitic structure (Oberlin, 1984; Oberlin et al. 1999). The natural and experimental kinetic

85   approaches on carbonization have been widely investigated using vitrinite reflectance (Hood et

86   al. 1975; Burnhan and Sweeney, 1989; Sweeney and Burnham, 1990; Huang 1996), biomarker

87   thermal maturity (Sheppard et al. 2015), carbon X-ray absorption near-edge structure

88   spectroscopy (C-XANES: Cody et al. 2008), micro-Raman spectroscopy (Muirhead et al. 2012)

89   and *in-situ* micro-Fourier transform infrared spectroscopy (Kebukawa et al. 2010). These kinetic

90   studies have reported wide ranges of apparent activation energies between 98 and 345 $kJmol^{-1}$

91   (Marsh et al. 1999), some of which are comparable to the dissociation energies of C–H bonds

92   (346–421 kJ mol^{-1}) and C–C bonds (254–346 kJ mol^{-1}). The other major process, graphitization,

93   involves crystallization from a turbostratic to a graphitic structure by the reorganization of

94   stacking sheets. The structural change of CM to graphite has been well studied using X-ray

95   diffraction (Grew 1974; Wada et al. 1994), transmission electron microscopy (Buseck and

96   Huang, 1985) and micro-Raman spectroscopy (Wopenka and Pasteris, 1993). On the other hand,

97   the experimental studies on the kinetics of graphitization are scarce in the literature. The biggest

98   drawback in synthesizing graphite is that it requires very high treatment temperature ($\sim$ 3000 K)

99   in a low fO_2 environment under ambient pressure. Early kinetic studies in the 1960s–1970s

100   already reported an effective activation energy of $\sim$ 1000 kJ mol^{-1} for the formation of graphite

101   (e.g., Fischbach 1963, 1971; Murty et al. 1969). These values are in good agreement with

102   activation energies of vacancy diffusion from experiments with natural graphite (Kanter, 1957)

103   and first principles calculation (Kaxiras and Pandey, 1988). However, such a high effective

104   activation energy based on experimental results points to notable differences between natural and

105   experimental structural evolution of CM. For instance, extrapolation based on previous

106   experimental kinetic data at 1 atm suggests that even at 700 °C, graphite would require durations

107   of the order 10^{40} min (1.9 $\times$ 10^{34} years; Fischbach 1971; Bustin et al. 1995). Therefore, it is

108   required that we should provide more realistic experimental kinetic model and more realistically

109   constrained experimental data to understand the kinetics behind natural graphitization.

110   The large divergence between experimental and natural graphitization results from

111   neglecting other factors such as lithostatic pressure (Noda et al. 1968; Beyssac et al. 2003),

112   tectonic deformation (Ross and Bustin, 1990; Bustin et al. 1995) and catalytic effects (Marsh et

113   al. 1983). This work constructs a revised kinetic model for natural graphitization through an

114   experimental exploration of the synthesis of graphite under relatively low temperature and

115   pressure conditions (1000–1450 °C and 1 GPa), when compared with early kinetic studies.

116   Previous studies on the synthesis of graphite have noted that the structural evolution of CM to

117   graphite depends greatly on the nanostructure of the precursor materials (graphitizing and

118   non-graphitizing carbon) (Oberlin 1984; Oberlin et al. 2006). Therefore, we used two different

119   CM samples extracted from representative pelitic rocks in a low-grade metamorphic terrain and

120 an accretionary complex to compare the influence of the nanostructure of the precursor. Our

121 findings lead to a revised kinetic model for the natural structural evolution of CM, which

122 advances our understanding of graphitization in natural environments over geological timescales.

123 The acronyms are described in Table 1.

124

125   **METHOD**

126

127 **Starting materials**

128 The natural CMs in pelitic rocks are complex aggregates of two CM end-members

129 (non-graphitizing and graphitizing carbon; Oberlin 1984). The heterogeneity of nanostructures is

130 one of the most important factors to discuss in the recrystallization during the high pressure high

131 temperature (HPHT) experiments. It is difficult to quantify the heterogeneity of nanostructures in

132 transmission electron microscopy observations and reconstruct the natural heterogeneity of CM

133 using the two end-members. Therefore, the starting materials for the HPHT experiments were

134 prepared from two different naturally occurring sedimentary rocks: one from the Hidaka

135 metamorphic belt (HMB) and the other from the Cretaceous Shimanto accretionary complex

136 (SM). Both starting materials extracted by HF-HCl treatments were expected to demonstrate

137 behavior closer to that in nature than observed in previous experiments using cokes and other

138 commercial carbon materials, and especially suitable starting materials, because their localities

139 have been well studied in terms of structural geology, metamorphic geology, and organic

140 geochemistry (Nakamura et al. 2015; Ohmori et al. 1997).

141   The CM in HMB were sampled from muscovite-chlorite grade metasediments, which

142 are located near to the boundary of the biotite isograd (see Nakamura et al. 2015 for detailed

143 geological relations). Under the microscope, the CM was observed along the grain boundaries of

144 quartz or plagioclase within pelitic layers, and along cleavage planes in chlorite and muscovite.

145 The CM showed a turbostratic (sample HMB, d_{002} spacing = 3.431 ± 0.007 Å) structure in XRD

146 profiles and high R2 ratio (R2 ratio = 0.62 ± 0.01) in micro-Raman spectroscopy.

147   The CM in SM were sampled from mudstone in the Hinotani unit of the Cretaceous

148 Shimanto accretionary complex. The Hinotani unit is dominated by coherent turbidite units

149 containing massive and bedded sandstone, interbedded sandstone and mudstone, and mudstone.

150 The CMs in this area show the lowest maturity and systematically change their crystallinity with

151 increasing the paleo-thermal gradient toward the out-of-sequence thrusts (Fukase fault and Aki

152 Tectonic line), ranging between 1.3 and 3.0 % of vitrinite reflectance (Ohmori et al. 1997). In

153 addition, these sediments are considered as a candidate precursor for high pressure metamorphic

154 rocks such as Sambagawa metamorphic belt (e.g., Aoki et al. 2011; low temperature high

155 pressure type metamorphic terrain). Therefore, these rocks have another benefit, to compare

156 different geothermal gradients in metamorphic regimes. Under the microscope, the CM was

157 identified optically as two different macerals (vitrinite and inertinite), and it coexists with illite,

158 plagioclase, quartz, and framboidal pyrite in pelitic layers. The CM showed an amorphous

159 (sample SM, d_{002} spacing = 3.505 ± 0.013 Å) structure in XRD profiles and a broad D1 band

160 FWHM in micro-Raman spectroscopy (D1 band FWHM = 129.4 ± 8.4 cm^{-1}). The two samples

161 we have selected cover a wide range of crystallinity, and are suitable for applying experimental

162 graphitization of natural CM back to the temperature–time scale of metamorphic rocks.

163

164 **Chemical extraction from pelitic rocks**

165 Given that the sedimentary rocks have low concentrations of organic carbon (total organic

166   carbon values of 0.3–0.7 wt%; Nakamura et al. 2015), we followed the chemical extraction for

167   preparing the required aliquots of CM samples (Nakamura and Akai, 2013). The presence of

168   silicate or oxide minerals in the starting materials may form various carbides at high temperature

169   (> 900 °C; e.g., Charon et al. 2014), therefore it is important to eliminate these minerals as much

170   as possible by chemical extraction.

171   The rock samples (500–800 g) were crushed by a Jaw crusher and sieved using a

172   200–mesh screen. The sieved powder was initially treated with 2N HCl to remove carbonate,

173   sulfide, sulfate and hydroxides (Vandenbroucke and Largeau, 2007), and then the solution was

174   treated by HF (48 %) in several large Teflon vessels (500 ml) and dried on a hot plate at 120 °C.

175   Dried residues in Teflon vessels were composed of CMs and newly formed fluorides such as

176   ralstonite and other complex fluorides (Durand and Nicaise, 1980). These fluorides are difficult

177   to redissolve once precipitated and they interfere with further analysis of CM (Vandenbroucke

178   and Largeau, 2007), therefore, we performed repeated rinsing with hot deionized water between

179   acid treatments (Durand and Nicaise, 1980). The residues were dissolved again in 2N HCl at 60

180   °C. The chemical treatments were repeated several times until the CM floated in the solution.

181   This floatation is a signal of the complete decomposition of fluorides (Itaya, 1981; Itaya 1985).

182   The supernatant of CM was filtered and dried on a watch glass. Note that the CM residues

183   retained small amounts of minerals such as zircon, rutile, ilmenite, and pyrite even after HF–HCl

184   acid treatments. Both starting materials of SM and HMB are slightly matured or metamorphosed

185   during diagenesis and low grade metamorphism, respectively. Many researchers have concluded

186   that the HF–HCl acid treatments do not alter the CM structure and do not generate newly formed

187   solvent soluble organic materials except in the case of very immature sediments (Durand and

188   Nicaise, 1980; Larsen et al. 1989; Vandenbroucke and Largeau, 2007).

189

HPHT experiments

HPHT experiments were performed at the Institute for Planetary Materials (IPM), Okayama University, Misasa, Japan. The two starting materials were encapsulated and stamped in platinum tubes of 2.0 and 3.0 mm outer diameter. Experiments were carried out with both starting materials together in a single run so as to reduce any apparent difference in absolute temperature conditions. After welding and encapsulating, the platinum capsules were placed in two different pressure apparatus for appropriate treatment of temperature and time; (1) The piston-cylinder (PC) apparatus (2) The DIA-type apparatus (AMAGAEL). For the PC experiments, the assembly was composed of a talc-Pyrex-graphite furnace with MgO disks as pressure medium (19.05 mm (3/4 inch diameter)). Two platinum capsules were placed at the center of graphite heater. Experimental temperature was measured by type S (Pt-Pt_{90}-Re_{10}) thermocouples. For experiments using the DIA-type apparatus, the cubic pyrophyllite with edge length of 21 mm was adopted as pressure medium and the tungsten carbide anvils with top edge length was 15 mm. Temperature was monitored using $W_{97}Re_3$-$W_{75}Re_{25}$ thermocouples with Al_2O_3 insulating sleeves, whose junction was placed in contact with the center of MgO disk. We used DIA-type apparatus for high temperature conditions (1325 and 1450 °C). Previous studies on HPHT experiments already reported that the conversion of graphite at 1 GPa required at least 1200 °C for 100 h (Beyssac et al. 2003). Therefore, our experiments were carried out at four different temperature conditions between 1000 °C and 1450 °C, and different annealing durations at peak temperature from 10 min to 115 h. Short experiments of 1s duration (PC 481 and PC 482) were also carried out for reference, however, these were not used for kinetic analysis due to uncertainties in time-temperature estimates. Both experiments were carried out

212   with a heating rate of about 100 °C / min and quenching by switching off the furnace power.

213

214   **Analytical methods**

215   The recovered platinum capsules were mounted into epoxy resin and cut into two halves. One

216   half was used for SEM observations and micro-Raman spectroscopy. The other half was

217   separated from the slab section of platinum capsule using a dentist diamond cutter under a

218   binocular microscope. The powder was used for X-ray diffraction and transmission electron

219   microscopy observations.

220   X-ray diffraction (XRD) was obtained using a Rigaku ULTIMA IV diffractometer at

221   Niigata University, equipped with CuKα (40 kV, 40 mA) radiation, graphite monochromator, slit

222   system 2/3 °–0.45 mm–2/3 ° and time constant of 0.5 ° min^{-1}. The diffractometer was run

223   between 10 ° and 90 °. The powdered samples of CM were dried on a Si-low background sample

224   holder with internal standard of silicon (10–20 wt%). Lattice constant and crystal thickness of

225   graphite were calculated according to the following methods. The 2θ values of the obtained

226   peaks were calibrated using the peak positions of the internal silicon standard (Iwashita et al.

227   2004). The $L_c(002)$ was calculated using the Scherrer equation: $L_c(002) = K\lambda / \beta\cos\theta$, where K,

228   constant (1.0); λ, X-ray wavelength (Cu$K\alpha$ = 1.5419 Å); β, full width at half maximum

229   (FWHM); θ, the Bragg angle. The K value is not a constant, but depends on the crystallite sizes

230   (Fujimoto 2003). Therefore, we used the constant K of 1.0 for $L_c(002)$ following JIS standards

231   (Iwashita et al. 2004).

232   Micro-Raman spectroscopy was applied to CM and graphite in the first order region

233   using a Jasco NRS 3100 spectrometer at Niigata University, equipped with the grating of 1800

234   lines/mm and CCD-detector (256×1024 pixels). The microscope objective of 100×, and

235 Nd-YAG laser (wavelength: 532 nm) were used. Acquisition time is 10–30 s, and 3–6 spectra

236 were cumulated for each data point. All Raman peak profiles were analysed by using peak

237 profile fitting, and G (1580 cm^{-1}), D1 (1350 cm^{-1}), D2 (1620 cm^{-1}), D3 (at around 1450 cm^{-1}),

238 and D4 (at around 1200 cm^{-1}) bands in the first order region (1000–1800 cm^{-1}) were separated.

239 The parameters of G band FWHM, D1 band FWHM, G position (Raman shift), R1 ratio

240 (Intensity $_{D1\ band}$ / Intensity $_{G\ band}$), R2 ratio (Area $_{D1\ band}$ / Area $_{G + D1 + D2\ bands}$), and Area ratio (AR;

241 Area $_{D1 + D4\ bands}$ / Area $_{G + D2 + D3\ bands}$) were estimated. The Tuinstra and Koenig equation were

242 applied: I_{D1} / I_G = C(λ) / L_a (nm) (Tuinstra and Koenig 1970); where C (λ), constant (4.4); I_{D1}/I_G,

243 Intensity $_{D1\ band}$ / Intensity $_{G\ band}$, R1 ratio; L_a (nm), the crystal size of lateral extent of carbon

244 sheets. Mean values and standard deviations were calculated based on 11–20 analyses for both

245 edge and center part of samples.

246   Scanning electron microscopic (SEM) observations were carried out using a JEOL

247 6510LA, equipped with an energy dispersive X-ray spectrometer (EDS) at Niigata University.

248 Both samples were observed without coating under low vacuum pressure.

249   Transmission electron microscopy (TEM) was carried out using a JEOL JEM 2010

250 electron microscope in Niigata University, operating at 200 kV with LaB$_6$ filament. CM samples

251 extracted from the run products were ground and suspended in pure water. After ultrasonic

252 cleaning in plastic tubes, the solution was deposited on the carbon-coated holey film of the TEM

253 micro-grid treated by plasma cleaning. The samples were mainly observed for the d_{002} lattice

254 fringe along the [010] direction.

255

256   **RESULTS**

257

Morphological characteristics of run products

Both CM samples show gradually changing surface optical properties (i.e., relative reflectance) as annealing occurs at increasing temperatures and for longer durations. Short annealing (1 s to 10 min) leads to the formation of many voids and cracks of 1 to 10 μm width in some areas of the run products (Fig. 1a). Such pores are rare in the HMB samples (Fig. 1b). Previous studies have also reported the presence of voids or porous structures on polished coal surfaces, suggesting the release of volatile matter from the precursor (Rodrigues et al. 2011; Zhou et al. 2014). Our observations also suggest a change in the bulk density of the CM due to the release of volatile matter during carbonization (Inagaki and Meyer 1999). In addition, the morphological characteristics of the CM gradually change in response to both annealing duration and temperature. Treatment at 1000 °C leads to CM samples consisting of small grains of 1–10 μm diameter with porous structures observable by SEM (Fig. 1c). Treatment at higher temperatures changes the CM to aggregates with planar structures (Fig. 1d), which do not show the hexagonal morphology commonly seen by SEM in well crystallized graphite.

XRD analysis

Both CM samples extracted from Pt capsules show systematically changing XRD profiles with respect to temperature and duration (Fig. 2a; Table 2). Crystal parameters derived from the XRD patterns reveal the evolution of three types of microstructure: amorphous (1D), turbostratic (2D), and graphitic (3D) structures. At the early stage (1 s to 10 min), SM shows a broad and symmetric reflection at the 2θ range of 40–45° in XRD profiles. This single broad reflection (named as 10 reflection) is a composite of d_{100} and d_{101} reflections, suggesting the presence of randomly oriented small stacks in amorphous structure. Longer annealing (1 to 6 h, Fig. 2a)

281 makes the broad peaks asymmetric owing to the formation of turbostratic structure. This

282 asymmetric peak starts to split into the d_{100} and d_{101} reflections with increasing temperature and

283 time. The d_{112} and d_{006} reflections also appear, suggesting the formation of a graphitic structure

284 (Fig. 2a). Both samples show such progressive structural changes from amorphous to graphitic

285 with increasing temperature.

286

287 **Micro-Raman spectroscopy**

288 Two prominent bands corresponding to the G band (1580 cm^{-1}) and D1 band (1350 cm^{-1}) appear

289 in the first-order region (1000–1800 cm^{-1}; Fig. 2b; Table A1). Their intensity and area ratio

290 gradually change with increasing temperature and longer treatment. In addition to the first-order

291 region, the overtone and combinations of the G and D bands (2D1, D1+G, 2D2) in the

292 second-order region (2500–3200 cm^{-1}) show similar changes to the main bands, as reported by

293 Wopenka and Pasteris (1993). At the early stage of annealing at low temperature, disordered

294 bands such as D3 and D4 are identified by the peak deconvolution of two prominent bands (Fig.

295 2b). The 1500 cm^{-1} D3 band generally appears broad, suggesting that it originates from

296 amorphous sp^2-bonded carbon from organic molecules, fragments, or functional groups in poorly

297 organized materials (Cuesta et al. 1994; Sadezky et al. 2005). The 1200 cm^{-1} D4 band is also

298 derived from poorly organized organic materials, and is attributed to sp^3–sp^2 mixed sites at the

299 peripheries of crystallites or to C–C and C=C stretching vibrations of polyene-like structures

300 (Dippel et al. 1999; Sadezky et al. 2005; Shen 2007). These two bands indicate that the CM

301 samples at the early stage of annealing at low temperatures have many dangling bonds on

302 polyaromatic layers. Higher temperatures and longer annealing change the CM into a graphitic

303 structure, as shown by the decreasing intensity of the disordered bands. These structural changes

304   observed by micro-Raman spectroscopy are in a good agreement with those observed by XRD.

305   Beyssac et al. (2003) reported that the crystal parameters in micro-Raman spectroscopy display

306   strong heterogeneous distributions in microscopic scale. To assess the microtextural

307   heterogeneity, we compared the area ratio of the center with the edge part of non-polished slab

308   section of platinum capsules (Fig. 3). The edges of both samples annealed at lower temperatures

309   show slightly lower crystallinity compared with the central part of the capsule. This may have

310   resulted from the temperature and microstructural heterogeneity within the assembly as reported

311   by Beyssac et al. (2003). However, almost all data obtained in the temperature range exhibited a

312   strong squared correlation coefficient of 0.978 in the center vs. the edge parts of area ratio plot

313   (Fig. 3).

314

315   **TEM observations**

316   The starting materials of HMB and SM show different microstructural signatures. Although the

317   CMs of HMB display broad 002, 10, and 11 rings in the selected area electron diffraction

318   (SAED) patterns, poorly crystallized parallel fringes are locally observed in the tissue-like

319   aggregates (Fig. 4a). Under high magnification, poorly organized fringes surrounded by

320   disordered graphitic layers are discernible. The distorted graphitic layers already have anisotropy

321   in lateral direction. The SAED pattern in the distorted graphitic layers shows arc-like spots of

322   002 reflections, suggesting turbostratic structures within graphitic layers (Fig. 4b). Such

323   aggregates of CM were also observed in the chlorite zone (Buseck and Huang, 1985). On the

324   other hand, the CMs of SM also show broad 002 rings in the SAED patterns and granular

325   aggregates (Fig. 4c). Under high magnification, poorly organized fringes that are composed of

326   2–3 carbon layers are observed. In contrast to the CM in HMB, the poorly organized fringes are

327   isotropically oriented in the aggregates (Fig. 4d). The isotropic distributions of poorly organized

328   fringes generally correspond to the nanostructure of BSU in coal (Oberlin et al. 1999). Longer

329   and higher-temperature annealing converts these nanostructures to a graphitic structure (Figs.

330   4e–h). Under the 11 dark-field (DF) mode, the platy graphite displays a typical Moiré fringe,

331   suggesting a fully ordered and stiff layer in lateral direction (Fig. 4e; Oberlin 1984). In addition,

332   the 10 ring in the SAED pattern starts to split into two diffraction patterns of 100 and 101 spots,

333   while the 11 ring splits into 110 and 112 spots (Fig. 4g). The lattice fringes of the d_{002} spacing

334   are fully ordered, and define (002) and (101) in the SAED pattern along the [010] direction (Figs.

335   4f and 4h). These microstructural observations suggest that heat treatment converted both CM

336   samples to a graphitic structure. However, the SAED patterns still display ring and spotted

337   patterns, suggesting the presence of turbostratic or amorphous structures in the graphitic carbon.

338   In fact, some of the XRD peak profiles show asymmetric d_{002} peaks, which included signatures

339   of both the turbostratic and graphitic components in the microstructure. Previous studies using

340   XRD (Inagaki and Meyer 1999), micro-Raman spectroscopy, and TEM observations (Beyssac et

341   al. 2003) have reported that graphitization under HPHT conditions induces heterogeneous

342   recrystallization. In this study, similar patterns regarding microstructural evolution observed by

343   TEM supports their results observed in XRD and micro-Raman spectra.

344

345   **Time–temperature relations inferred from heat treatment**

346   The time–temperature relations of both CM samples display changes in crystallinity with

347   increasing annealing duration (Figs. 5a–l). Similar to the observations of Beyssac et al. (2003),

348   structural changes at 1000 °C were limited when annealing lasted between 10 min and 48 h.

349   However, structural changes of CM to graphite occurred at 1200, 1325, and 1450 °C as the heat

350 treatment progressed. In particular, almost all the crystal parameters indicated a graphitic

351 structure even at the early stage of heating (1 to 6 h), and most of the parameters became

352 constant or showed only extremely slow change after 6 h, suggesting either the termination of

353 crystal growth or only sluggish growth. In addition, each parameter obtained from XRD and

354 micro-Raman spectroscopy displays some important signatures in the time–temperature

355 relations. The d_{002} spacing (Figs. 5a and 5d) and FWHM (Figs. 5b and 5e) for both CM samples

356 terminate at around 3.36 Å and 0.4 °, respectively. The $L_c(002)$ of SM (Fig. 5f) also indicates the

357 termination of crystal growth at around 200 Å, whereas that of HMB (Fig. 5c) still grow up over

358 200 Å in crystal thickness. The unchanging d_{002} spacing indicates the formation of graphitic

359 structures in the microstructures, but the termination of crystal growth shows a different

360 signature from both samples. In general, the final crystal sizes of carbon materials such as carbon

361 black and soft carbon directly depends on the primary nanostructures (spherical or platy) during

362 graphitization (Inagaki 1996). The starting material of SM displayed isotropic poorly organized

363 fringes (Fig. 4d), whereas that of HMB already had developed the anisotropic distorted layers

364 (Figs. 4a and 4b). The different primary nanostructures considered here may have influenced the

365 final crystal sizes and morphological characteristics of the run products.

366

367 **DISCUSSION**

368

369 **Kinetic models of graphitization**

370 The results of the HPHT experiments at 1 GPa for both CM samples suggest that their changes in

371 crystallinity, morphology, and nanostructures were directly related to both the duration and

372 temperature of treatment. We therefore assessed three different kinetic approaches of

373 graphitization using the power rate model (e.g., Murty et al. 1969), the Johnson-Mehl-Avrami

374 (JMA) model (e.g., Sung 2001; Khawam and Flanagan, 2006) and the superposition method

375 (e.g., Fischbach 1963; Inagaki et al. 1968). Before we adopted these kinetic models, the

376 experimental data were converted to the degree of graphitization (g) by following the equation

377 (Murty et al. 1969; Khawam and Flanagan, 2006; Table 2):

378 $$g = (d_0 - d_1) / (d_0 - d_f), \quad (1)$$

379 where d_0 is the initial value of d_{002} spacing (Figs. 5a and 5d; Fischbach, 1971), d_1 is the observed

380 experimental data, and the d_f show the final value of d_{002} spacing (Figs. 5a and 5d; Fischbach,

381 1971). The power rate model is the most robust kinetic model for carbonization and widely

382 applied for extrapolating the geological time-temperature regime using the rate constant and

383 pre-exponential factor (e.g., Huang 1996). After conversions to nondimensional parameters, we

384 attempted to fit the following power law of time as:

385 $$g = k_p t^{-n}, \quad (2)$$

386 where k_p is the rate constant, t time (s), n an order of reaction at that temperature. The

387 experimental data fitted by the equation (2) show squared correlation coefficient of 0.584–0.952

388 depending on the treatment temperatures (Figs. 6a–b). The rate constant k_p and order of reaction

389 n also demonstrate distributions as a function of the treatment temperature. In particular, the

390 logarithm of rate constant lnk_p and order of reaction n show strong squared correlation

391 coefficient of 0.979 (Fig. 7). This suggests that the kinetics of graphitization under low and high

392 temperature underwent different chemical reactions. Some previous studies have used the mean

393 values of order of reaction (Huang 1996) or linear regression values from the least squares of

394 experimental data (Muirhead et al. 2012) to avoid the experimental uncertainty of the complex

395 chemical reactions. The differences of experimental uncertainty are permissible in the range of

396   order of reaction (n) between 0.062 and 0.09 (Huang, 1996). On the other hand, the orders of

397   reaction in this study vary widely ($n = 0.007$ to 0.82), and it is difficult to apply the previous

398   methods directly (Fig. 7). The results imply that graphitization is not a simple chemical reaction

399   and that various reactions progress simultaneously (concurrent reaction) and/or successively

400   (successive reaction). In this study, we attempted to fit the Arrhenius relation using following

401   equation:

402   $$k_{p,} = A\exp(-E_a/RT), \qquad (3)$$

403   where k_p is the rate constant, A the pre-exponential factor, E_a the effective activation energy, R

404   the gas constant, and T the absolute temperature of the experiment. Using the Arrhenius equation

405   (3), we calculated the effective activation energy. The values of SM and HMB samples partly

406   demonstrate good squared correlation coefficients of 0.903 and 0.981, however, have a large

407   uncertainty spread in the average of activation energies of $259 \pm 26 \, \text{kJ} \, \text{mol}^{-1}$ and 271

408   $\pm 63 \, \text{kJ} \, \text{mol}^{-1}$ (Fig. 6c; Table 3). Consistent with the results of earlier experimental studies, we

409   concluded that graphitization does not follow a simple power rate model (e.g., Fischbach 1971).

410   Instead of a power rate model, we tried to calculate the best fitting using a JMA model

411   to apply for the complex "sigmoid" transformation from an amorphous to a graphitic structure

412   (Figs. 5a-l). The JMA equation is suitable to heterogeneous nucleation and recrystallization and

413   widely applied in material science (e.g., Khawam and Flanagan, 2006). The equation was

414   expressed as follows:

415   $$g = 1 - \exp(-k_a t^l), \qquad (4)$$

416   where k_a is the rate constant of JMA equation, l is the order of reaction named for "Avrami

417   index", t is the duration of heating (s). Taking the natural logarithm of equation (4), it can be also

418   expressed as:

19

$$\ln[-\ln(1 - g)] = \ln k_a + l \ln t, \qquad (5)$$

Plotting the left side of equation ($\ln[-\ln(1 - g)]$) and natural logarithm of time $\ln t$, the rate constant k_a and Avrami index l are estimated from the linear regression of intercept and slope in this Avrami plot, respectively. The model fitting by a JMA equation displays squared correlation coefficient between 0.555 and 0.963 depending on the temperatures (Figs. 6d–e). The rate constant k_a and order of reaction l also demonstrate distributions as a function of the temperature (Fig. 7). Such variations are consistent with the results of the power rate model, suggesting complex chemical reactions. Using the $\ln k_a$ values vs. $1/T$, we obtained the effective activation energies of 269 ± 59 kJ mol^{-1} and 273 ± 47 kJ mol^{-1} for HMB and SM samples, respectively (Fig. 6f; Table 3). Both models are not in good agreement with the experimental structural changes from CM to graphite. These misfits to model fitting result from the large variation of the effective activation energies. Thus, we concluded that the structural change of CM to graphite cannot follow a simple power rate model nor a simple JMA model.

We therefore applied the superposition method to propose a kinetic model for natural graphitization. The effective activation energy is usually obtained from the slope of the Arrhenius plot, which is the logarithm of the rate constant vs. the reciprocal of absolute temperature (i.e., $\ln k$ vs. $1/T$). Arrhenius plots using a power rate model and a JMA model empirically provide only one intercept value ($\ln k$) for each treatment temperature, whereas the superposition method has an advantage in its determination of the activation energy using two or more slopes derived from all experimental data. This is an effective method to predict the kinetics of complex chemical reactions. The superposition method is well known to describe the mechanical and electrical relaxation behavior of polymers, and some earlier studies have successfully applied the Arrhenius approach to graphitization (e.g., Fischbach 1971; Feng et al.

442   2002). The fitting curves of the measured crystal parameters vs. the logarithmic treatment time at

443   different temperatures can be superposed by proper scale changes on the time axis. The shift in

444   distance is called the time–temperature shift factor a_T, which is given by:

445                                    $a_T = t_T / t_{ref},$ (6)

446   where t_{ref} is the reference time at a certain reference temperature (Fig. 8a), and t_T is the time

447   required to give the same response at the reference temperature (Fig. 8a). For every reference

448   temperature chosen, a fully superimposed curve generated by the shift factors is called the master

449   curve. The above equation (6) also can be written by combining the Arrhenius equation (3):

450                            $a_T = \exp\{E_a/R \ (1/T - 1/T_{ref})\},$ (7)

451   where both T and T_{ref} are absolute temperatures. Plotting $\ln(a_T)$ vs. $1/T$ is another way to

452   calculate E_a values and to predict crystal changes at low temperatures. The crystal properties

453   with regression curves obtained by the superposition method are shown in Figure 8 and Table 4.

454   The experimental reference temperature here is 1000 °C. To find the best-fitting non-linear

455   regression curve, some sigmoid functions and power functions were chosen to determine the

456   shift values (Table 4). The fitting considered four parameters: the unit-cell height c, the FWHM

457   of the d_{002} peak, $L_c(002)$, and the area ratio of the Raman bands. The master curves obtained for

458   both samples show good squared correlation coefficients of 0.878 to 0.982 (Figs. 8a–d; Table 4).

459   In particular, these sigmoid functions accurately reflect the three different processes of the

460   successive reactions from carbonization to graphitization. The first stage of heat treatment

461   corresponds to the formation of BSUs by the release of aliphatic and aromatic C–H bonding.

462   After devolatilization, they start to crystallize from turbostratic to graphitic structures as the

463   temperature and duration increase. The final transformation to graphite suggests the termination

464   of crystal growth. Our extrapolations using sigmoid fitting have an advantage over the linear or

465   power law fitting models used in previous studies, because we can extrapolate from the starting

466   point to the termination point using a single sigmoid master curve. The effective activation

467   energy was calculated from the relationship between $\ln(a_T)$ and $1/T$. The plot of the mean values

468   and their linear regression lines show good squared correlation coefficients of 0.984–0.999

469   (Table 4), suggesting that the relation between annealing duration and temperature can be

470   described as a thermal activation process. The mean values of effective activation energies were

471   274 ± 9 and 339 ± 6 kJ mol^{-1} for HMB and SM, respectively (Fig. 9).

472   The estimated activation energies between 259 and 339 kJ mol^{-1} using a power rate

473   model, a JMA model and a superposition method are remarkably lower than the previously

474   determined activation energies (~ 1000 kJ mol^{-1}) under 1 atm. Summarizing the previous studies

475   and our results, we found that the effective activation energies systematically decrease as a

476   function of pressure (Fig. 10). Some previous studies pointed out that the structural evolution of

477   CM to graphite rapidly progress by additional pressure (Beyssac et al., 2003; Zhao et al. 2009).

478   However, these studies only noted the possibility of fast graphitization under high pressure and

479   detailed investigation of kinetics under high pressure is limited. Noda et al. (1968) argued that

480   graphitization under high pressure changes the E_a values from 1000 kJ mol^{-1} to

481   330–500 kJ mol^{-1} by additional pressure of 0.3–0.5 GPa. Such a large pressure dependence on

482   graphitization was also observed in this study. According to the results of Lynch and Drickamer

483   (1966) and Hanfland et al. (1989), the crystal thickness (L_c) and diameter (L_a) in a graphitic

484   structure decrease by about 2.2 % and 0.17 % at 1 GPa at room temperature, respectively. The

485   interlayer spacing of graphite decreases by about 2.5 % with development of the graphitic

486   structure. Thus, the decrease at 1GPa is comparable to the total decrease of interlayer spacing

487   during graphitization. Such a large effect on compression along the c-axis may result from a

488 "negative" activation volume under HPHT experiments. In the light of pressure dependence, the

489 activation energy under high pressure is strictly expressed by the equation: $\Delta H = \Delta Ea + P\Delta V^{\neq}$,

490 where ΔH is the activation enthalpy, ΔEa the activation energy at 1 atm, P the pressure, $\Delta V^{\neq}$ the

491 activation volume. If the ΔH values are correlatable to a single effect on pressure dependence,

492 the ΔEa values and pressure P will show a linear relationship, and the ΔH and $\Delta V^{\neq}$ values can be

493 calculated from the intercept and slope, respectively. In this study, the relation between the

494 effective activation energy and pressure seems to display a logarithmic curve rather than a linear

495 regression line (Fig. 10). This may suggest that the different factors are included in the whole

496 "effective" activation energies. For instance, Marsh et al. (1983) reported that catalytic effects

497 largely change the activation energy from 1000 kJ mol^{-1} to ~ 400 kJ mol^{-1} without addition of

498 pressure. Although it is uncertain to calculate the activation volume using our results, we found

499 that the activation energies between ambient pressure and 1 GPa decrease by a factor of over 2.

500 Thus, almost all natural graphitization in the earth's crust undergoes a faster transformation than

501 estimated in previous studies.

502

503 **IMPLICATIONS**

504

505 Our experimental kinetic study on the structural evolution of CM to graphite gave remarkably

506 low activation energies for the natural precursor materials, and natural graphitization in the

507 Earth's crust may proceed much more quickly than suggested by previous calculations based on

508 large activation energies (~ 1000 kJ mol^{-1}) because of "negative" activation volume during

509 graphitization. This suggests that extrapolation using our kinetic model at 1 GPa is expected to

510 model well the conditions of geological environments and produce better results than previous

511   studies. Based on the experimental results in this study, we attempted a simplified isothermal

512   calculation of graphitization rate depending on temperature. If graphitization rate is subject to

513   Arrhenian temperature dependence, the sigmoid master curves can be extrapolated to represent

514   low-temperature conditions. For instance, sigmoid fitting was tested using the parameters of

515   unit-cell height c, and the area ratio (AR) of Raman spectra:

$$f(t) = C_{min} + (C_{max} - C_{min}) \, / \, \{1 + (t_{half}/t)^h\}, \quad (8)$$

517   where C_{min} and C_{max} are respectively the maximum and minimum values of each parameter, t is

518   the annealing duration during metamorphism, t_{half} is the inflection point obtained from this

519   function, and h is the order of reaction of the sigmoid function (called "Hill coefficient"). The

520   values of C_{min} and C_{max} correspond to the starting and termination points of natural

521   graphitization, respectively, and h is used for the experimental data (Table 4). The value of t_{half}

522   changes as functions of time and temperature. Therefore, we calculate its value at target

523   temperature and time from the Arrhenius plots. The t_{half} can also be described following the

524   Arrhenius relation:

$$t_{half} = A_1 \exp(-m/T), \qquad (9)$$

526   where A_1 is the intercept and m is the slope of the Arrhenius plot. Combining equation (8) and

527   (9):

$$f(T, t) = C_{min} + (C_{max} - C_{min}) \, / \, [1 + \{A_1\exp(-m/T)/t\}^h], \qquad (10)$$

529   It is thus possible to predict the structural evolution of CM to graphite by the above function of

530   peak temperature T (K) and annealing duration t (min) during metamorphism. Using the above

531   equation (10), we attempted to extrapolate the structural evolution of CM to graphite at low

532   temperatures (300–800 °C) during annealing for 10^0–10^{10} years. For instance, the master curve at

533   1000 °C extended to ~ 10^6 min (~ 2 years) for the formation of graphite (Figs. 8a–d). With

534   decreasing temperature, the time required for conversion to graphite exponentially increases.

535   Figure 11 shows the calculated time–temperature transformation diagrams using the parameters

536   of unit-cell height c (Figs. 11a and 11c) and the area ratio (AR) of Raman spectra (Figs. 11b and

537   11d). If CM in HMB underwent prograde metamorphism for about 10,000 years, it would show

538   initial crystallinity changes at $\sim$ 500 °C and conversion to the fully ordered graphite (d_{002} spacing

539    $\sim$ 3.36 Å) at over $\sim$ 640 °C (Path 1 of Fig. 11a). Longer metamorphism for $\sim$1 m.y. would

540   convert CM to fully ordered graphite at temperatures over $\sim$ 520 °C (Path 2 of Fig. 11a). The CM

541   in SM shows a similar change in its crystallinity as a function of duration (Path 5 and 6 of Fig.

542   11c), however, the estimated temperatures at the conversion of graphite are slightly higher than

543   that in HMB. This difference results from the difference in the initial activation energy required

544   to form a graphite. Wang (1989) reported that almost fully ordered graphite (d_{002} spacing $\sim$ 3.36

545   Å) in high-pressure low-temperature and high-temperature low-pressure metamorphic rocks can

546   form at temperatures between 410 and 440 °C in various metamorphic terrains. Our kinetic

547   model suggests that annealing following metamorphism requires $\sim 10^8$ years (Fig. 11a). The

548   results are not in good agreement with natural and calculated graphitization rates. In addition to

549   unit-cell height c, the area ratio (AR) in HMB and SM also displays similar behavior as a

550   function of heating duration (Figs. 11b and d). If CM in HMB underwent prograde

551   metamorphism for about 10,000 years, it would show initial crystallinity changes at 350 °C and

552   conversion to graphite (AR < 0.2) at over 800 °C (Path 3 of Fig. 11b). Longer metamorphism for

553    $\sim$ 1 m.y. would convert CM to graphite at temperatures over $\sim$ 720 °C (Path 4 of Fig. 11b). The

554   CM in SM displays initial crystallinity changes at 350 °C and conversion to graphite at over

555   590 °C for duration of $\sim$ 1 m.y. (Path 8 of Fig. 11d). In contrast to the unit-cell height c, the

556   contour of AR tends to extend over a wide interval in time-temperature space (Figs. 11b and d).

557   The difference is driven by the calculated Hill coefficient h in equation (10), making AR a more

558   sensitive measure for graphitization progress over a wide temperature range. In the case of

559   micro-Raman spectroscopic studies, almost all CM changed into graphite at around 650 °C based

560   on the detailed observations of various types of metamorphic terrains (Beyssac et al. 2002; Aoya

561   et al. 2010; Hilchie and Jamieson 2014). If CMs changed into graphite at 650 °C by

562   graphitization, the durations of heating required would be about 100,000 years (SM) and 10 m.y.

563   (HMB), respectively. These estimations suggest that natural CMs are rapidly able to change their

564   crystallinity as functions of realistic duration and peak temperature. In particular, the structural

565   change of CMs in SM are consistent with previously reported examples of natural graphitization

566   (Beyssac et al. 2002; Aoya et al. 2010), where crystallinity increased at temperature between 350

567   and 650 °C. This suggests that the Raman spectra of carbonaceous materials (RSCM)

568   thermometry have potential to be calibrated to use the Arrhenius-type t-T-dependence of

569   graphitization as a tool for extracting kinetic information from natural rocks. On the other hand,

570   we found that the two CM samples display a large divergence of recrystallization. This

571   difference results from the sigmoid t-T-relation descried by the Hill coefficient h, and suggests

572   that further detailed evaluation of the chemical reaction under natural and laboratory conditions

573   are required for a complete understanding of structural evolution of CM.

574   Overall, our kinetic model demonstrates that graphitization can proceed at relatively low

575   temperatures (520 ~ 720 °C) in generally more realistic timescales (~ 1 m.y.) than expected from

576   previous experimental kinetic studies (e.g., Fischbach 1971). In addition, our new kinetic data

577   suggests that activation energies as reported previously (e.g., Fischbach 1971) do not suitably

578   describe natural graphitization in crustal settings. Under a lithostatic pressure of 1 GPa, we were

579   able to demonstrate the structural evolution of CM at geologically reasonable temperatures

580   (300–800 °C) and durations ($1-10^{10}$ years). Further refining and a better understanding of the

581   kinetics of graphitization might provide new pathway to use it not only as a tool for

582   geothermometry but also for geospeedometry in order to resolve petrogenetic processes

583   occurring over geologic timescales. However, there exist slight mismatch between our

584   experimental results and natural graphitization in metamorphic rocks. It can be deduced that the

585   actual activation energies for natural graphitization could be even slightly lower than that

586   estimated here due to the influence of other factors (e.g., catalytic effects, tectonic deformation

587   and fluid activity), and further experiments will help to constrain the influence of additional

588   factors to refine our kinetic model for natural graphitization.

589

590   **ACKNOWLEDGEMENTS**

591

604

605   **REFERENCE CITED**

606

607   Aoki, K., Maruyama, S., Isozaki, Y., Otoh, S., and Yanai, S. (2011) Recognition of the Shimanto

608   HP metamorphic belt within the traditional Sanbagawa HP metamorphic belt: New

609   perspectives of the Cretaceous–Paleogene tectonics in Japan. Journal of Asian Earth Sciences,

610   42, 355–369. doi:10.1016/j.jseaes.2011.05.001

611   Aoya, M., Kouketsu, Y., Endo, S., Shimizu, H., Mizukami, T., Nakamura, D., and Wallis, S.

612   (2010) Extending the applicability of the Raman carbonaceous-material geothermometer

613   using data from contact metamorphic rocks. Journal of Metamorphic Geology, 28, 895–914.

614   http://doi.wiley.com/10.1111/j.1525-1314.2010.00896.x

615   Beyssac, O., Brunet, F., Petitet, J.-P., Goffé, B., and Rouzaud, J.-N. (2003) Experimental study

616   of the microtextural and structural transformations of carbonaceous materials under pressure

617   and   temperature.   European   Journal   of   Mineralogy,   15,   937–951.

618   http://dx.doi.org/10.1127/0935-1221/2003/0015-0937

619   Beyssac, O., Goffé, B., Chopin, C., and Rouzaud, J.N. (2002) Raman spectra of carbonaceous

620   material in metasediments: a new geothermometer. Journal of Metamorphic Geology, 20,

621   859–871. http://doi.wiley.com/10.1046/j.1525-1314.2002.00408.x

622   Buseck, P.R., and Beyssac, O. (2014) From Organic Matter to Graphite: Graphitization.

623   Elements, 10, 421–426. DOI: 10.2113/gselements.10.6.421

624   Buseck, P.R., and Huang, B.-J. (1985) Conversion of carbonaceous material to graphite during

625   metamorphism.   Geochimica   et   Cosmochimica   Acta,   49,   2003–2016.

626   doi:10.1016/0016-7037(85)90059-6

627   Bustin, R.M., Rouzaud, J.-N., and Ross, J.V. (1995) Natural graphitization of anthracite:

628   Experimental considerations. Carbon, 33, 679–691. doi:10.1016/0008-6223(94)00155-S

629   Burnham, A.K., and Sweeney, J.J. (1989) A chemical kinetic model of vitrinite maturation and

630   reflectance.   Geochimica   et   Cosmochimica   Acta,   53,   2649–2657.

631   doi:10.1016/0016-7037(89)90136-1

632   Charon, E., Rouzaud, J.-N., and Aléon, J. (2014) Graphitization at low temperatures (600–1200

633   °C) in the presence of iron implications in planetology. Carbon, 66, 178–190.

634   doi:10.1016/j.carbon.2013.08.056

635   Cody, G.D., Alexander, C.M.O.D., Yabuta, H., Kilcoyne, a L.D., Araki, T., Ade, H., Dera, P.K.,

636   Fogel, M.L., Militzer, B., and Mysen, B.O. (2008) Organic thermometry for chondritic parent

637   bodies. Earth and Planetary Science Letters, 272, 446–455. doi:10.1016/j.epsl.2008.05.008

638   Cuesta, A., Dhamelincourt, P., Laureyns, J., Martínez-Alonso, A., and Tascón, J.M.D. (1994)

28

639 Raman microprobe studies on carbon materials. Carbon, 32, 1523–1532.
640 doi:10.1016/0008-6223(94)90148-1

641 Dippel, B., and Heintzenberg, J. (1999) Soot characterization in atmospheric particles from
642 different sources by NIR FT Raman spectroscopy. Journal of Aerosol Science, 30,
643 S907–S908. doi:10.1016/S0021-8502(99)80464-9

644 Durand, B., and Nicaise, G., (1980) Procedures of kerogen isolation. Kerogen, Insoluble Organic
645 Matter from Sedimentary Rocks. 35–53 p. Editions Techiq, Paris.

646 Feng, B., Bhatia, S.K., and Barry, J.C. (2002) Structural ordering of coal char during heat
647 treatment and its impact on reactivity. Carbon, 40, 481–496.
648 doi:10.1016/S0008-6223(01)00137-3

649 Fischbach, D.B. (1963) Kinetics of graphitization of a petroleum coke. Nature, 200, 1281–1283.
650 doi:10.1038/2001281a0

651 Fischbach, D.B. (1971) The kinetics and mechanism of graphitization. The Chemistry and
652 Physics of Carbon, 1–154 p. Marcel Dekker, New York.

653 Fujimoto, H. (2003) Theoretical X-ray scattering intensity of carbons with turbostratic stacking
654 and AB stacking structures. Carbon, 41, 1585–1592. doi:10.1016/S0008-6223(03)00116-7

655 Grew, E. G. (1974) Carbonaceous Material in Some Metamorphic Rocks of New England and
656 Other Areas. The Journal of Geology, 82, 50–73. http://www.jstor.org/stable/30068626

657 Hanfland, M., Beister, H., and Syassen, K. (1989) Graphite under pressure: Equation of state and
658 first-order Raman modes. Physical Review B, 39, 12598–12603.
659 DOI:http://dx.doi.org/10.1103/PhysRevB.39.12598

660 Hilchie, L.J., and Jamieson, R.A. (2014) Graphite thermometry in a low-pressure contact
661 aureole, Halifax, Nova Scotia. Lithos, 208-209, 21–33. doi:10.1016/j.lithos.2014.08.015

662 Hood, A., Gutjahr, C.C.M., and Heacock, R.L. (1975) Organic Metamorphism and the
663 Generation of Petroleum. AAPG Bulletin, 59, 986–996.

664 Huang, W.-L. (1996) Experimental study of vitrinite maturation: effects of temperature, time,
665 pressure, water, and hydrogen index. Organic Geochemistry, 24, 233–241.
666 doi:10.1016/0146-6380(96)00032-0

667 Inagaki, M. (1996) Carbon materials structure, texture and intercalation. Solid State Ionics,
668 86-88, 833–839. doi:10.1016/0167-2738(96)00337-2

669 Inagaki, M., and Meyer, R.A. (1999) Stress graphitization. The Chemistry and Physics of

670   Carbon, 149–243 p. Marcel Dekker, New York.

671 Inagaki, M., Murase, Y., and Noda, T. (1968) Effect of Pre-Heat-Treatment on Kinetics of

672   Graphitization. Journal of the Ceramic Association, Japan, 76, 184–189.

673   http://doi.org/10.2109/jcersj1950.76.874_184

674 Itaya, T. (1981) Carbonaceous material in pelitic schists of the Sanbagawa metamorphic belt in

675   central Shikoku, Japan. Lithos, 14, 215–224. doi:10.1016/0024-4937(81)90043-8

676 Itaya T. (1985) Rapid separation technique of carbonaceous materials from a lot of

677   meta-sedimentary rocks. Bulletin of the Hiruzen Research Institute, Okayama University of

678   Science 11, 47–57 (in Japanese with English abstract).

679 Iwashita, N., Park, C.R., Fujimoto, H., Shiraishi, M., and Inagaki, M. (2004) Specification for a

680   standard procedure of X-ray diffraction measurements on carbon materials. Carbon, 42,

681   701–714. doi:10.1016/j.carbon.2004.02.008

682 Khawam, A., and Flanagan, D.R. (2006) Solid-State Kinetic Models: Basics and Mathematical

683   Fundamentals. The Journal of Physical Chemistry B, 110, 17315–17328. DOI:

684   10.1021/jp062746a

685 Kanter, M. A. (1957) Diffusion of carbon atoms in natural graphite crystals. Physical Review,

686   107, 655–663. DOI: http://dx.doi.org/10.1103/PhysRev.107.655

687 Kaxiras, E., and Pandey, K. (1988) Energetics of defects and diffusion mechanisms in graphite.

688   Physical Review Letters, 61, 2693–2696. DOI:http://dx.doi.org/10.1103/PhysRevLett.61.2693

689 Kebukawa, Y., Nakashima, S., and Zolensky, M.E. (2010) Kinetics of organic matter

690   degradation in the Murchison meteorite for the evaluation of parent-body temperature history.

691   Meteoritics   and   Planetary   Science,   45,   101–115.

692   http://doi.wiley.com/10.1111/j.1945-5100.2009.01008.x

693 Kouketsu, Y., Mizukami, T., Mori, H., Endo, S., Aoya, M., Hara, H., Nakamura, D., and Wallis,

694   S. (2014) A new approach to develop the Raman carbonaceous material geothermometer for

695   low-grade   metamorphism   using   peak   width.   Island   Arc,   23,   33–50.

696   http://doi.wiley.com/10.1111/iar.12057

697 Larsen, J.W., Pan, C.S., and Shawver, S. (1989) Effect of demineralization on the

698   macromolecular structure of coals. Energy & Fuels, 3, 557–561. DOI: 10.1021/ef00017a004

699 Luque, F.J., Pasteris, J.D., Wopenka, B., Rodas, M., and Barrenechea, J.F. (1998) Natural fluid

700   deposited graphite: Mineralogical characteristics and mechanism of formation. American

701   Journal of Science, 298, 471–498.

702   Lynch, R.W., Drickamer, H.G., (1966) Effect of high pressure on the Lattice parameter of

703   diamond, graphite, and Hexagonal boron nitride. The Journal of Chemical Physics, 44,

704   181–184.

705   Marsh, H., Crawford, D., and Taylor, D.W. (1983) Catalytic graphitization by iron of isotropic

706   carbon from polyfurfuryl alcohol, 725–1090 K. A high resolution electron microscope study.

707   Carbon, 21, 81–87. doi:10.1016/0008-6223(83)90160-4

708   Marsh, H., Martínez-Escandell, M., and Rodríguez-Reinoso, F. (1999) Semicokes from pitch

709   pyrolysis: mechanisms   and   kinetics.   Carbon,   37,   363–390.

710   doi:10.1016/S0008-6223(98)00205-X

711   Muirhead, D.K., Parnell, J., Taylor, C., and Bowden, S.A. (2012) A kinetic model for the

712   thermal evolution of sedimentary and meteoritic organic carbon using Raman spectroscopy.

713   Journal of Analytical and Applied Pyrolysis, 96, 153–161. doi:10.1016/j.jaap.2012.03.017

714   Murty, H.N., Biederman, D.L., Heintz, E.A. (1969) Kinetics of Graphitization–I. Activation

715   energies. Carbon, 7, 667–681. http://dx.doi.org/10.1016/0008-6223(69)90522-3.

716   Nakamura, Y., and Akai, J. (2013) Microstructural evolution of carbonaceous material during

717   graphitization in the Gyoja-yama contact aureole: HRTEM, XRD and Raman spectroscopic

718   study.   Journal   of   Mineralogical   and   Petrological   Sciences,   108,   131–143.

719   http://doi.org/10.2465/jmps.120625

720   Nakamura, Y., Oohashi, K., Toyoshima, T., Satish-Kumar, M., and Akai, J. (2015)

721   Strain-induced amorphization of graphite in fault zones of the Hidaka metamorphic belt,

722   Hokkaido, Japan. Journal of Structural Geology, 72, 142–161. doi:10.1016/j.jsg.2014.10.012

723   Noda, T., Kamiya, K., and Inagaki, M. (1968) Effect of Pressure on Graphitization of Carbon. I.

724   Heat Treatment of Soft Carbon under 1, 3 and 5 kbar. Bulletin of the Chemical Society of

725   Japan, 41, 485–492. http://doi.org/10.1246/bcsj.41.485

726   Oberlin,   A.   (1984)   Carbonization   and   Graphitization.   Carbon,   22,   521–541.

727   doi:10.1016/0008-6223(84)90086-1

728   Oberlin, A., Bonnamy, S., and Oshida, K. (2006) Landmarks for graphitization. TANSO, 2006,

729   281–298. http://doi.org/10.7209/tanso.2006.281

730   Oberlin, A., Bonnamy, S., and Rouxhet, P.G. (1999) Colloidal and supermolecular aspect of

731   carbon. The Chemistry and Physics of Carbon, 1–148 p. Marcel Dekker, New York.

31

Ohmori, K., Taira, A., Tokuyama, H., Sakaguchi, A., Okamura, M., and Aihara, A. (1997) Paleothermal structure of the Shimanto accretionary prism, Shikoku, Japan: Role of an out-of-sequence thrust. Geology, 25, 327–330. doi: 10.1130/0091-7613(1997)

Rodrigues, S., Suárez-Ruiz, I., Marques, M., Camean, I., and Flores, D. (2011) Microstructural evolution of high temperature treated anthracites of different rank. International Journal of Coal Geology, 87, 204–211. doi:10.1016/j.coal.2011.06.009

Ross, J. V., and Bustin, R. (1990) The role of strain energy in creep graphitization of anthracite. Nature, 343, 58–60. doi:10.1038/346183a0

Sadezky, A., Muckenhuber, H., Grothe, H., Niessner, R., and Pöschl, U. (2005) Raman microspectroscopy of soot and related carbonaceous materials: Spectral analysis and structural information. Carbon, 43, 1731–1742. doi:10.1016/j.carbon.2005.02.018

Schwab, V., Spangenberg, J.E., and Grimalt, J.O. (2005) Chemical and carbon isotopic evolution of hydrocarbons during prograde metamorphism from 100°C to 550°C: Case study in the Liassic black shale formation of Central Swiss Alps. Geochimica et Cosmochimica Acta, 69, 1825–1840. doi:10.1016/j.gca.2004.09.011

Sheng, C. (2007) Char structure characterised by Raman spectroscopy and its correlations with combustion reactivity. Fuel, 86, 2316–2324. doi:10.1016/j.fuel.2007.01.029

Sheppard, R.E., Polissar, P.J., and Savage, H.M. (2015) Organic thermal maturity as a proxy for frictional fault heating: Experimental constraints on methylphenanthrene kinetics at earthquake timescales. Geochimica et Cosmochimica Acta, 151, 103–116. doi:10.1016/j.gca.2014.11.020

Sung, J. (2000) Graphite->diamond transition under high pressure: A kinetics approach. Journal of Materials Science, 35, 6041–6054. DOI: 10.1023/A:1026779802263

Sweeney, J. and Burnham A. K. (1990) Evaluation of a simple model of vitrinite reflectance based on chemical kinetics. AAPG Bulletin, 74, 1559–1570.

Tuinstra, F., and Koenig, L. (1970) Raman Spectrum of Graphite. The Journal of Chemical Physics, 53, 1126–1130. http://dx.doi.org/10.1063/1.1674108

Vandenbroucke, M., and Largeau, C. (2007) Kerogen origin, evolution and structure. Organic Geochemistry, 38, 719–833. doi:10.1016/j.orggeochem.2007.01.001

Wada, H., Tomita, T., Matsuura, K., Iuchi, K., Ito, M., and Morikiyo, T. (1994) Graphitization of carbonaceous matter during metamorphism with references to carbonate and pelitic rocks of

763   contact and regional metamorphisms, Japan. Contributions to Mineralogy and Petrology, 118,

764   217–228. DOI: 10.1007/BF00306643

765   Wang, G.-F. (1989) Carbonaceous material in the Ryoke metamorphic rocks, Kinki district,

766   Japan. Lithos, 22, 305–316. doi:10.1016/0024-4937(89)90032-7

767   Wopenka, B., and Pasteris, J.D. (1993) Structural characterization of kerogens to granulite-facies

768   graphite: Applicability of Raman microprobe spectroscopy. American Mineralogist, 78,

769   533–557.

770   Zhou, Q., Xiao, X., Pan, L., and Tian, H. (2014) The relationship between micro-Raman spectral

771   parameters and reflectance of solid bitumen. International Journal of Coal Geology, 121,

772   19–25. doi:10.1016/j.coal.2013.10.013

773   Zhao, J., Yang, L., Li, F., Yu, R., and Jin, C. (2009) Structural evolution in the graphitization

774   process of activated carbon by high-pressure sintering. Carbon, 47, 744–751.

775   doi:10.1016/j.carbon.2008.11.006

776

777   **TABLE and FIGURE captions**

778

779   **TABLE 1.** Summary of acronyms.

780

781   **TABLE 2.** Experimental conditions and XRD parameters of the run products at 1 GPa.

782   *Note:* $L_c(002)$ is calculated by the Scherrer equation ($K = 1.0$).

783   $g*$ (%) is the calculated degree of crystallinity using initial and final values of d_{002} spacing.

784

785   **TABLE 3.** Summary of rate parameters calculated from power rate and Johnson-Mehl-Avrami

786   models.

787

788   **TABLE 4.** Summary of calculated *Ea* values and fitting results.

789   *Note:* [a]$f(t) = A\exp(bt) + c$, [b]$\ln A_1$ is calculated from the intercept of the Arrhenius plot of $1/T$ and

790   $\ln t_{half}$. *Both C_{max} of area ratio is held.

791

792   **FIGURE 1.** Optical and backscattered images of the run products extracted from various

793   time–temperature experiments. **(a)** Photomicrograph of a polished slab section of sample PC

794   472SM showing many voids and cracks (1000 °C, 1 GPa, 1 s). **(b)** Photomicrograph of the

795   smooth surface of sample PC 461HMB (1200 °C, 1 GPa, 115 h). **(c)** Porous structure of powder

796   CM extracted from the Pt capsule for sample PC470SM (1000 °C, 1 GPa, 48 h). **(d)** Planar

797   structure of powder CM extracted from the Pt capsule for sample PC461HMB (1200 °C, 1 GPa,

798   115 h).

799

800   **FIGURE 2.** Structural evolutions from 1 s to 24 h of CM and starting material in SM to graphite

801   at 1450 °C as observed by **(a)** X-ray diffractometry and **(b)** micro-Raman spectroscopy. The

802   Raman spectra of CM are fitted by five peaks of D1, D2, D3, D4, and G band. Silicon peaks in

803   XRD profile are an internal standard for calibrating the interlayer spacing of disordered graphite.

804

805   **FIGURE 3.** Relationship between center and edge parts of area ratio (D1 + D4 bands) / (D2 +

806   D3 + G bands). The dashed line is calculated by linear regression.

807

808   **FIGURE 4.** Microstructural evolutions of the CM in HMB and SM to graphite. **(a)** TEM image

809   and corresponding SAED pattern of the starting material in HMB. The distorted graphitic layers

810   are locally observed in the tissue-like aggregates. **(b)** High-magnification image of the poorly

811   crystalline carbon surrounded by the distorted graphitic layers. The SAED pattern is compiled

812   from the area outlined by the white square. **(c)** TEM image and corresponding SAED pattern of

813   the starting material in SM. **(d)** High-magnification image and SAED pattern of poorly organized

814   fringes. **(e)** TEM image of ordered graphite and its 11 dark-field image (PC461HMB, 1200 °C

815   and 115 h). **(f)** Lattice fringes of graphite corresponding to (002) and (101) along the [010]

816   direction. **(g)** Nanostructures and corresponding SAED pattern of ordered graphite (A2584SM,

817   1200 °C and 48 h). **(h)** Lattice fringes and corresponding SAED pattern of ordered graphite.

818

819   **FIGURE 5.** Time–temperature relations between 10 and 10^4 min. The parameters **(a)** d_{002}

820   spacing, **(b)** FWHM of d_{002} peak, and **(c)** $L_c(002)$ from XRD, and also **(g)** D band FWHM, **(h)** G

821   band FWHM, and **(i)** area ratio are based on data for the CM in HMB. **(d)**, **(e)**, **(f)**, **(j)**, **(k)**, and

822   **(l)** show the same parameters, respectively, for the CM in SM. Data from XRD are used to

823   calculate the non-linear best fitting of sigmoid functions and power functions for reference.

824

825   **FIGURE 6.** The relationship between experimental $\ln t$ (s) and $\ln g$ of HMB **(a)** and SM samples

826   **(b)** fitted by a power rate model. **(c)** Arrhenius plot of HMB and SM samples. The relationship

827   between experimental $\ln t$ and $\ln[-\ln(1-g)]$ of HMB **(d)** and SM samples **(e)** fitted by a JMA

828   model. **(f)** Arrhenius plot of HMB and SM samples.

829

830   **FIGURE 7.** The relationship between the rate constants $\ln k_{p,a}$ and the orders of reaction n, l of

831   power rate and JMA models. All of rate constants and orders of reaction including d_{002} spacing,

832   FWHM of d_{002} peak, $L_c(002)$, and Area ratio and are plotted.

833

834   **FIGURE 8.** Composite master curves for CM samples SM and HMB obtained by shifting the

835   1200, 1325 and 1450 °C curves to combine smoothly with the 1000 °C (reference temperature)

836   curve from time–temperature relations. All master curves are calculated by non-linear best fitting

837   of sigmoid functions and power functions. Master curves of both CM samples are fitted by the

838   values of **(a)** unit-cell height c, **(b)** FWHM of d_{002} peak, **(c)** $L_c(002)$, and **(d)** area ratio.

839

840   **FIGURE 9.** Arrhenius plot of shift values using the average of four different parameters by

841   XRD and micro-Raman spectroscopy. Error bars show one standard deviation.

842

843   **FIGURE 10.** Compilation of effective activation energies (kJ mol^{-1}) at various pressures (GPa)

844   obtained in this study and published values using power rate model, JMA model and

845   superposition method. The effective activation energies of previous studies are cited from 1,

846   Fischbach (1963); 2, Inagaki et al. (1968); 3, Noda et al. (1965); 4, Fischbach (1971) 5, Murty et

847   al. (1969); 6, Noda et al. (1968); and 7, Marsh et al. (1983).

848

849   **FIGURE 11.** Time–temperature–transformation diagram of HMB **(a)** and SM samples **(c)** using

850   the unit-cell height c (Å). Orange area indicates the first appearance of fully ordered graphite

851   (d_{002} spacing ~ 3.36 Å) as reported by Wang (1989). Numerals indicate the unit-cell height c (Å),

852   which is contoured at an interval of 0.01 Å. Time–temperature–transformation diagram of HMB

853   **(b)** and SM samples **(d)** using the area ratio of (D1 + D4 bands) / (D2 + D3 + G bands).

854   Numerals indicate the area ratio, which is contoured at an interval of 0.1. Green area indicates

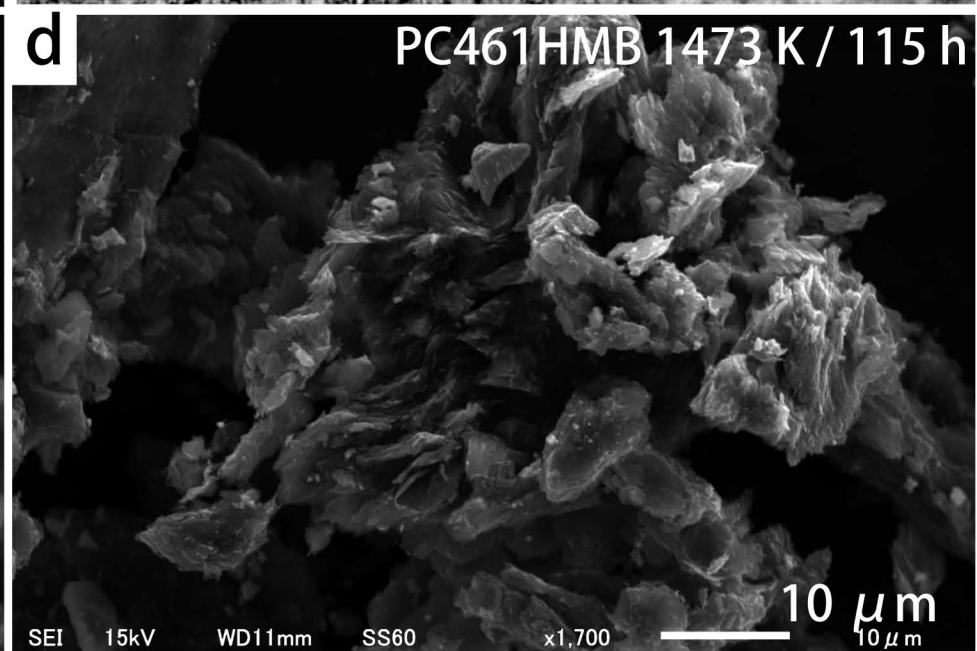855   the range of intersection at 650 °C.

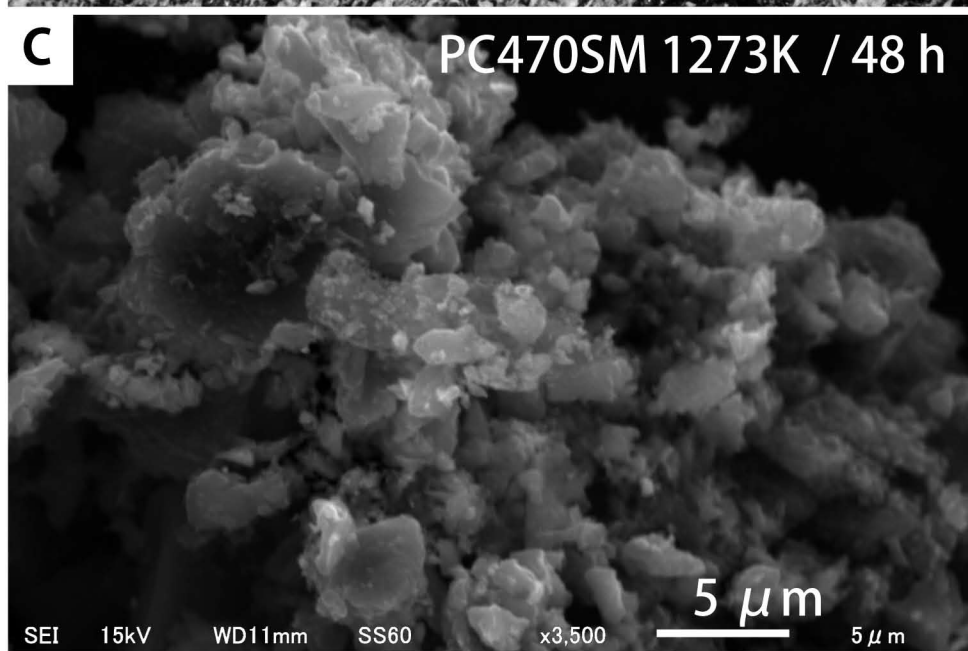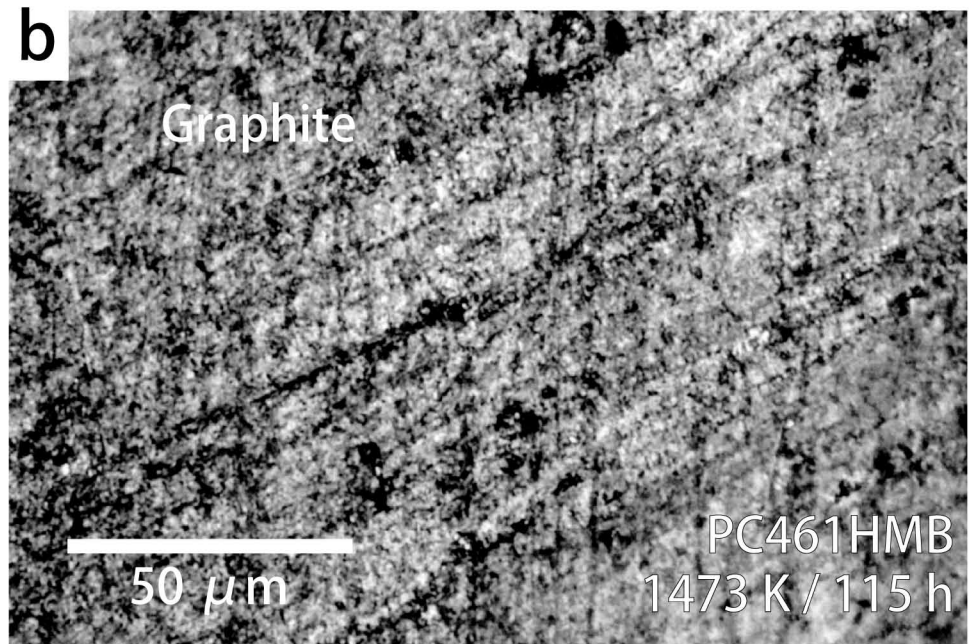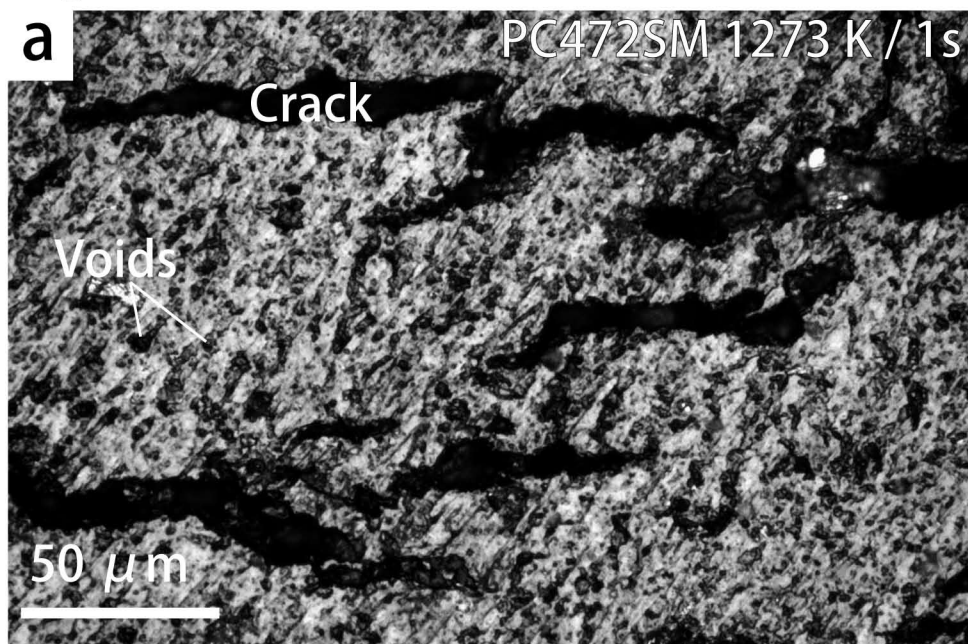35

856

APPENDIX

858

859   **TABLE A1.** Micro-Raman spectroscopic data for center and edge parts of CM obtained by peak

860   deconvolution.

861   *Note:* AR is the area ratio of (D1 + D4 bands) / (D2 + D3 + G bands).

862

Figure 1 2 column width
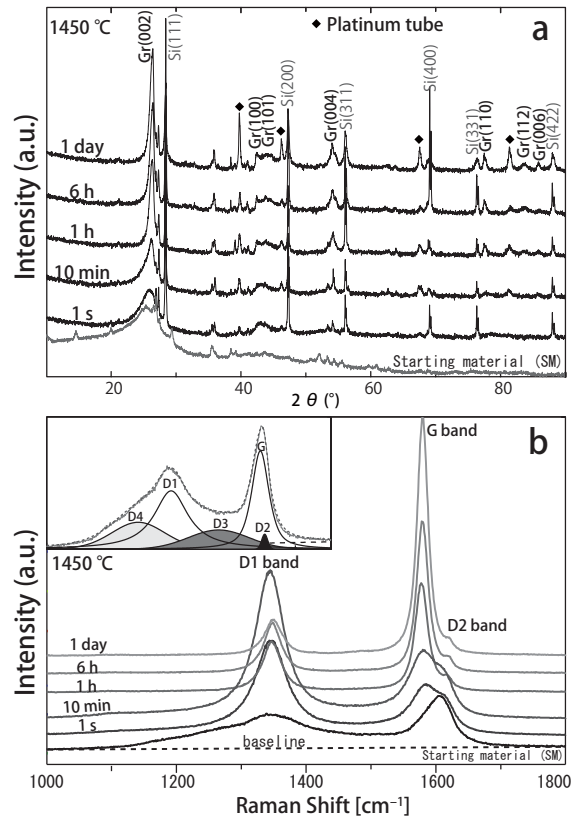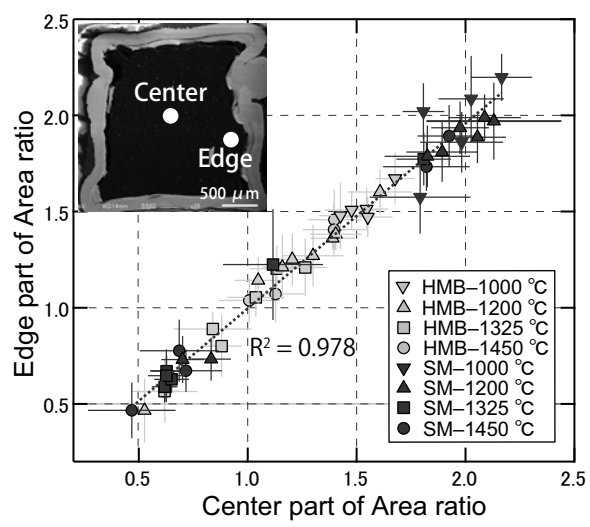
Figure 2 1 column width (76.2 mm × 110.6 mm)

Figure 3   1 column width (76.2 * 68mm)

Figure 4   2 column width

a — HMB (starting material) — 400 nm
Poorly crystallized parallel fringes
002 10 11

b — HMB (starting material) — 20 nm
c* c* 002

c — SM (starting material) — 200 nm
002 10 11

d — SM (starting material) — 10 nm
002 ring

e — PC461HMB 1473K / 115h — 200 nm
11 DF
Platy graphite

f — PC461HMB 1473K / 115h
c* 101
a*
3.4 Å   2.1 Å

g — A2584SM 1723 K / 24h — 200 nm
112
110
101
002
100
Platy graphite

h — A2584SM 1723 K / 24h — 10 nm
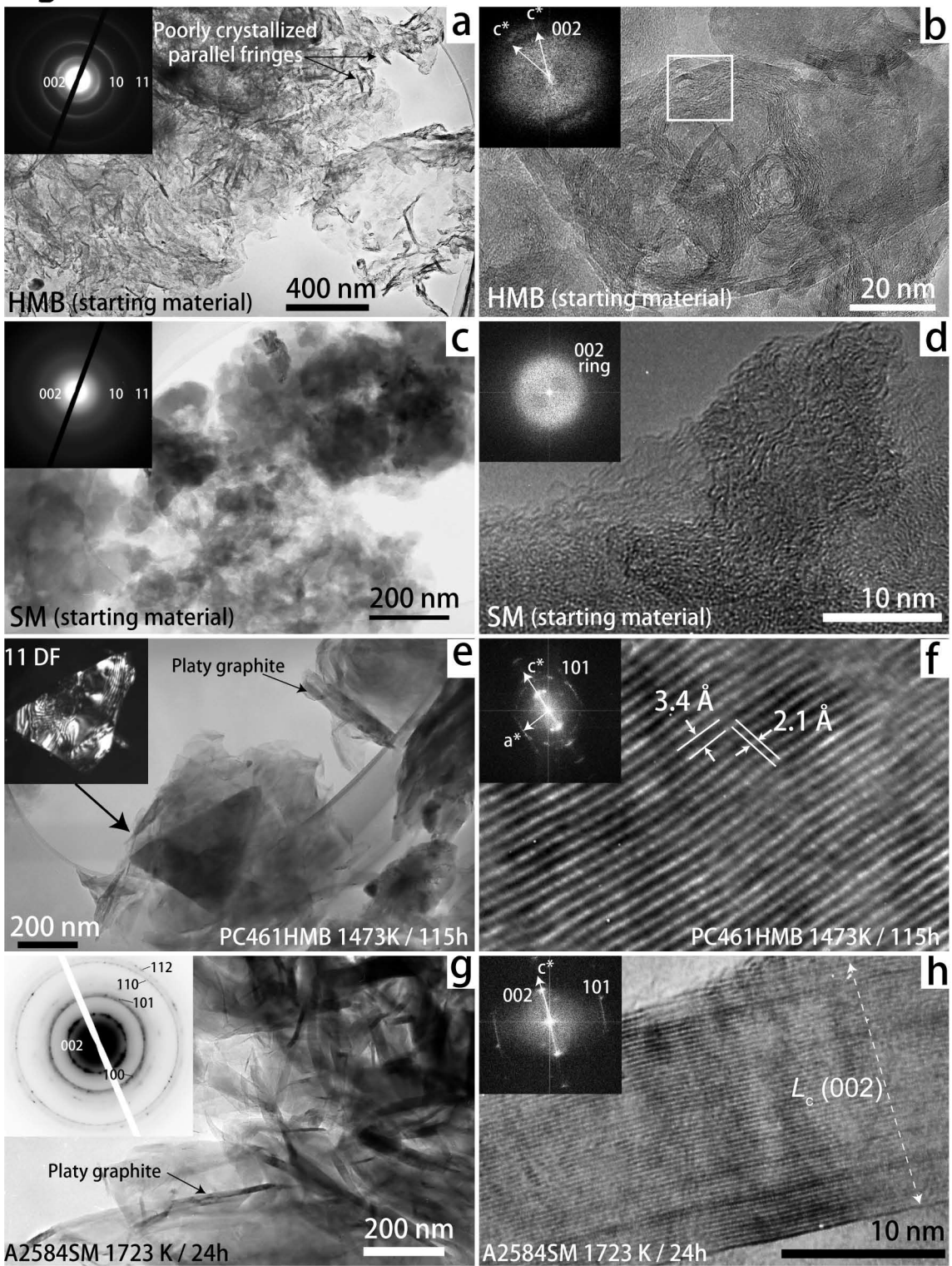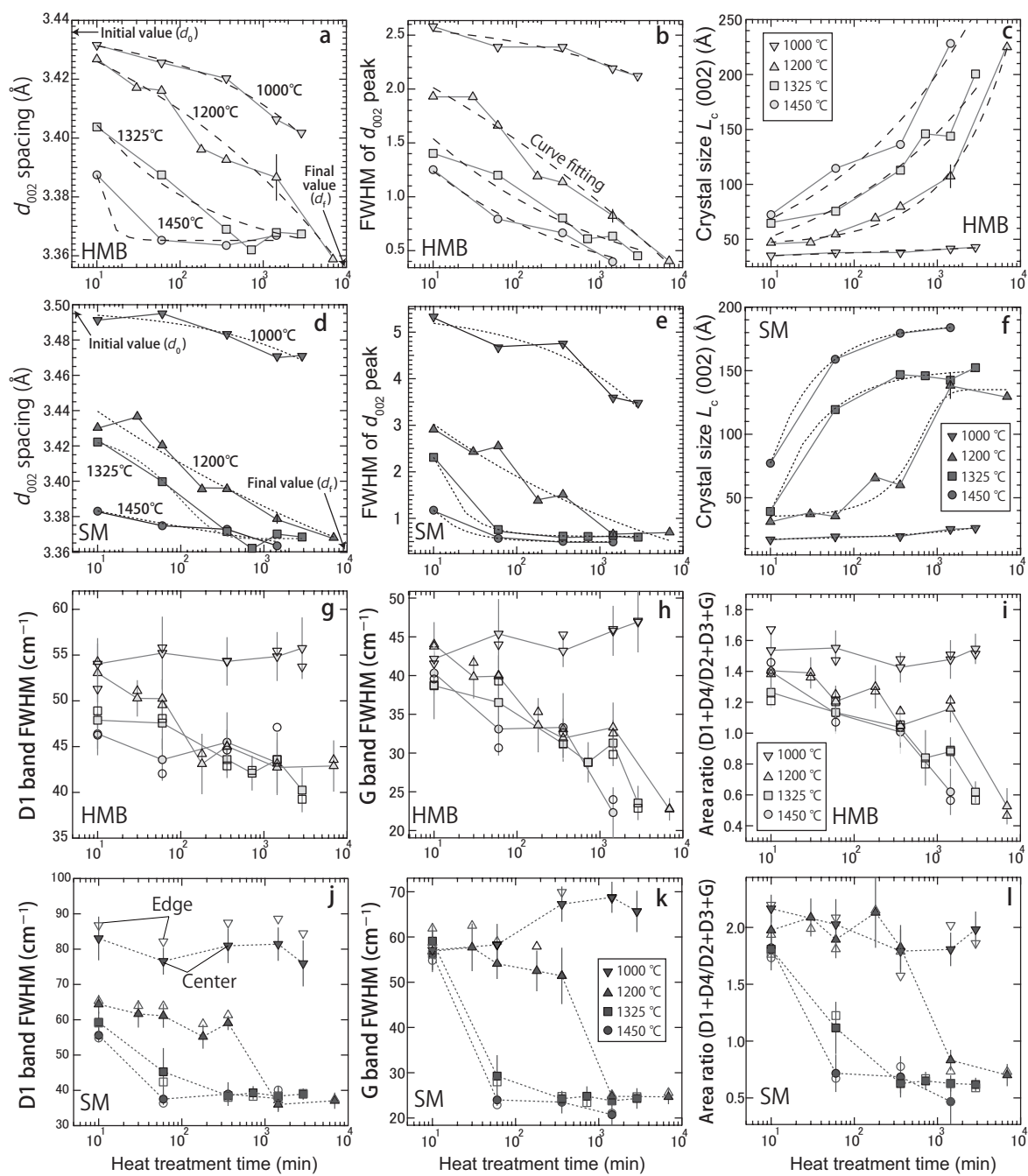c*
002 101
L_c (002)

Figure 5   2 column width (165mm × 182 mm)
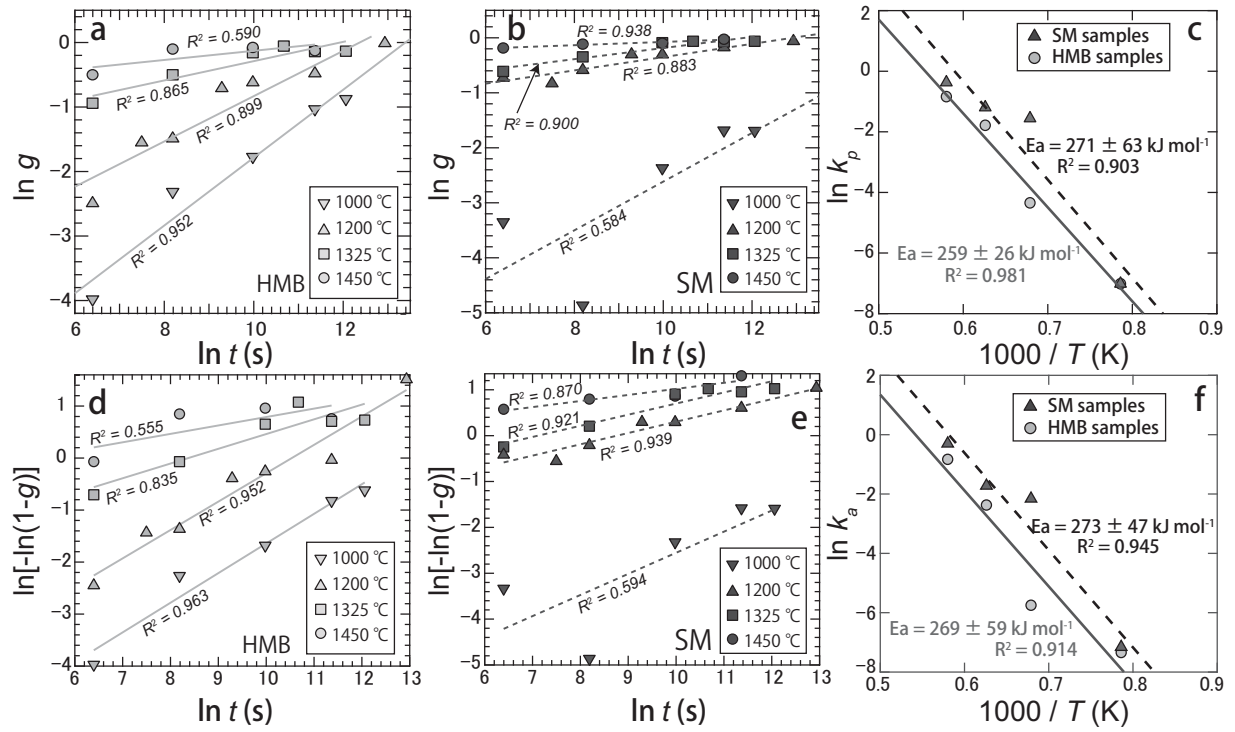
Figure 6   2 column width (165* 100 mm)
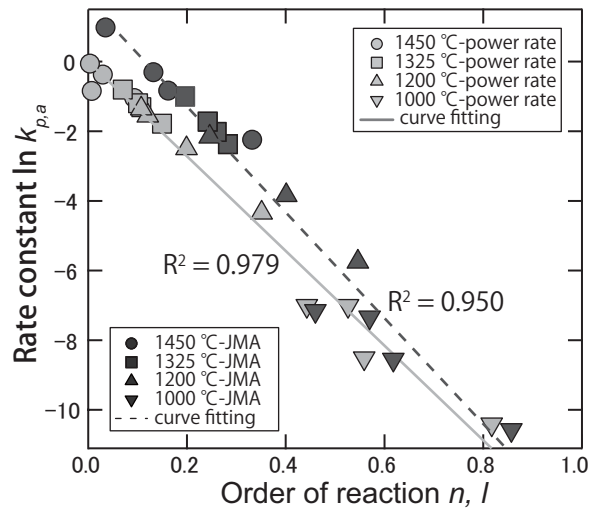
Figure 7   1 column width (76.2*66.6mm)

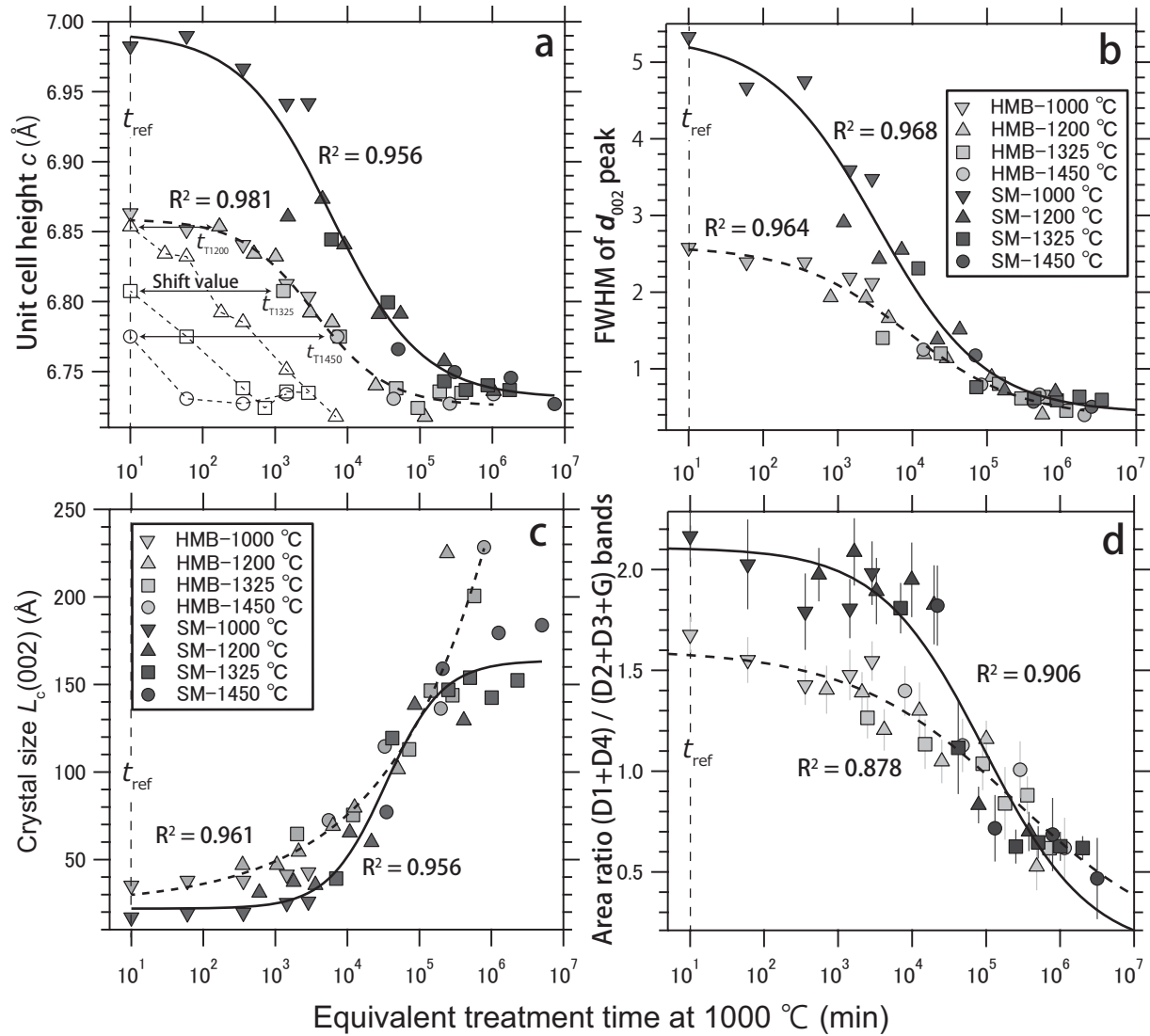# Figure 8   2 column width (165*150 mm)

Figure 9   1 column width (76.2 * 65.5mm)

Figure 10   1 column width (76.2* 70 mm)
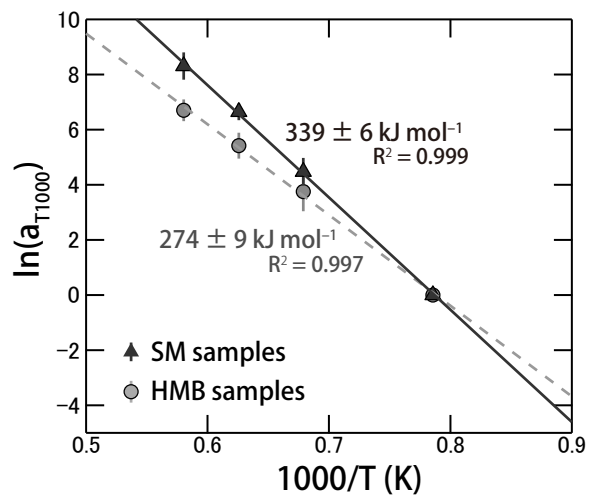
Figure 11   2 column width (165*121 mm)
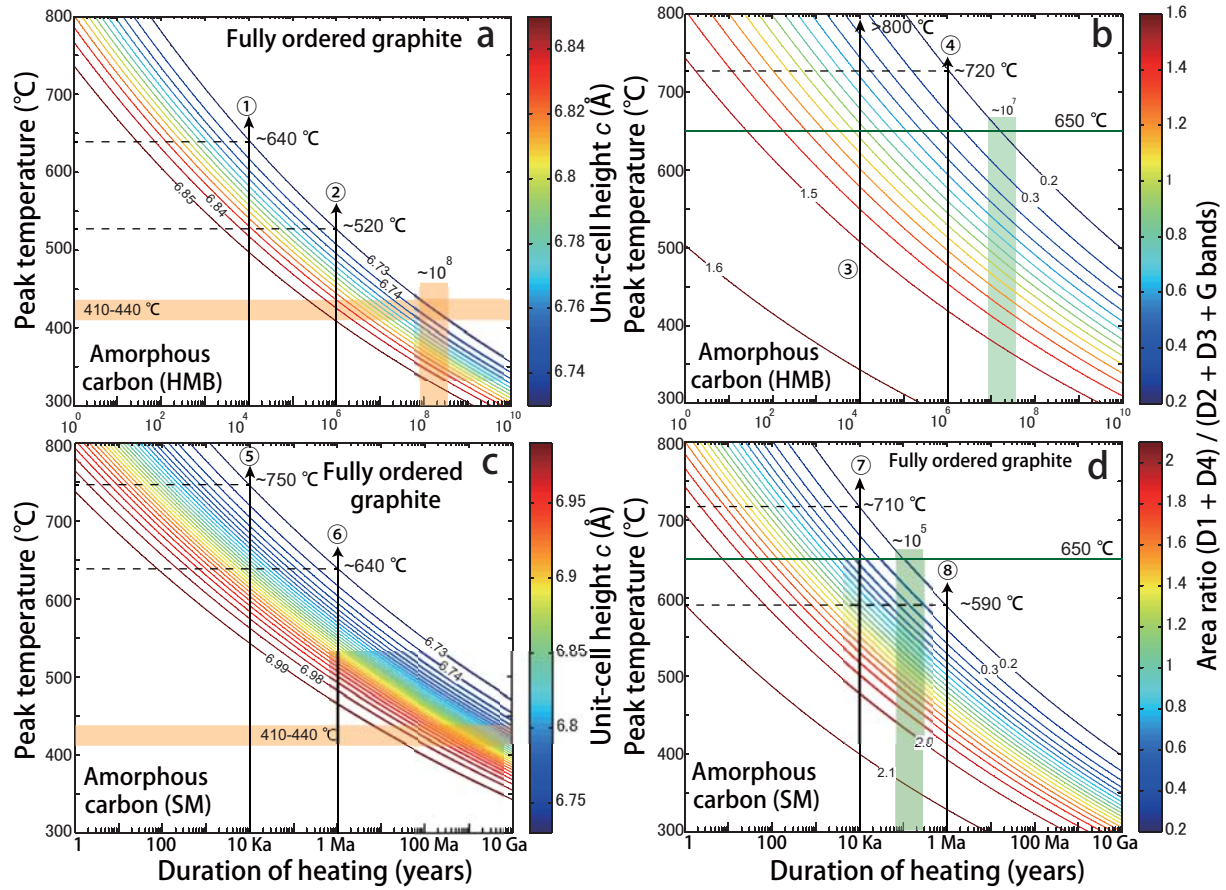
TABLE 1. Summary of acronyms

Acronym	Meaning
CM	Carbonaceous material
HMB	Hidaka Metamorphic Belt
SM	Shimanto accretionary complex
R1	Intensity ratio of (D1 / G) bands in Raman spectroscopy
R2	Area ratio of D1 / (D2 + D3 + G) bands in Raman spectroscopy
AR	Area ratio of (D1+D4) / (D2 + D3 + G) bands in Raman spectroscopy
d_{002}	Interlayer spacing of (002) in graphitic structure
FWHM	Full Width at Half Maximum
L_c (002)	Crystal thickness of graphite along c-axis
L_a	Lateral extent of carbon sheets
SAED	Selected Area Diffraction Pattern
BSU	Basic Structure Unit
JMA	Johnson-Mehl Avrami model

TABLE 2. Experimental conditions and XRD profiles of the run products at 1GPa

Run No.	Temp (°C)	Time (min)	d_{002} (Å)	FWHM	$L_c(002)$ (Å)	g^* (%)	d_{002} (Å)	FWHM	$L_c(002)$ (Å)	g^* (%)
			CM in Hidaka metamorphic belt				CM in Shimanto accretionary complex			
PC478	1000	10	3.432	2.58	35	0.019	3.491	5.33	17	0.035
PC475	1000	60	3.426	2.39	38	0.099	3.495	4.67	19	0.008
PC473	1000	360	3.420	2.39	38	0.170	3.483	4.75	20	0.093
PC471	1000	1440	3.406	2.19	41	0.356	3.471	3.59	25	0.186
PC470	1000	2880	3.402	2.12	43	0.416	3.471	3.48	26	0.184
PC482	1200	0.017	3.430	2.45	37	0.044	3.436	4.04	22	0.439
PC477	1200	10	3.427	1.93	47	0.083	3.430	2.91	31	0.483
PC479	1200	30	3.417	1.93	47	0.212	3.437	2.43	37	0.436
PC476	1200	60	3.416	1.66	55	0.226	3.420	2.55	36	0.556
PC485	1200	180	3.396	1.19	69	0.492	3.396	1.38	65	0.739
PC474	1200	360	3.393	1.14	80	0.538	3.396	1.51	60	0.738
PC462	1200	1440	3.387	0.89	107	0.619	3.382	0.72	127	0.840
PC461	1200	6900	3.359	0.40	225	0.989	3.368	0.70	129	0.941
A2590	1325	10	3.404	1.40	65	0.390	3.422	2.31	39	0.543
A2588	1325	60	3.387	1.20	76	0.607	3.400	0.76	119	0.708
A2583	1325	360	3.369	0.80	113	0.853	3.372	0.62	147	0.915
A2581	1325	720	3.362	0.61	146	0.947	3.368	0.64	154	0.938
A2582	1325	1440	3.368	0.63	144	0.868	3.370	0.59	143	0.926
A2580	1325	2880	3.367	0.45	201	0.875	3.368	0.60	152	0.938
PC481	1450	0.017	3.407	1.47	62	0.351	3.425	1.17	37	0.523
A2589	1450	10	3.388	1.25	72	0.607	3.383	0.57	77	0.831
A2587	1450	60	3.365	0.79	115	0.903	3.375	0.55	159	0.891
A2586	1450	360	3.364	0.67	136	0.927	3.373	0.51	179	0.906
A2584	1450	1440	3.367	0.40	228	0.881	3.363	0.49	184	0.975

Note: $L_c(002)$ is calculated by the Scherrer equation ($K = 1.0$)

g^* (%) is the calculated degree of crystallinity using initial and final values of d_{002} spacing

TABLE 3. Summary of rate paramters calculated from power rate and JMA models

Crystal parameter	Kinetic model	m	$\ln A$ (s)	Ea ($kJmol^{-1}$)	R^2
d_{002} spacing-HMB	power rate	−31103 (3070)	17.27 (2.06)	259 (26)	0.981
d_{002} spacing-SM	power rate	−32569 (7560)	19.21 (5.08)	271 (63)	0.903
d_{002} spacing-HMB	JMA	−32414 (7040)	17.50 (4.73)	269 (59)	0.914
d_{002} spacing-SM	JMA	−32886 (5620)	19.12 (3.78)	273 (47)	0.945

TABLE 4. Summary of calculated E_a values and fitting results

Parameters	Samples	Fitting data (sigmoid function)					Arrhenius plots				
		C_{min}	C_{max}	h	t_{half}	R^2	m	$\ln A$	$\ln A_1$ [b]	E_a (kJ mol^{-1})	R^2
d_{002} spacing	HMB	6.859 (6)	6.724 (4)	0.88 (14)	3577	0.982	−31893 (2230)	24.86	−16.680	265 (19)	0.990
FWHM	HMB	2.60 (14)	0.36 (14)	0.57 (12)	8482	0.964	−35641 (2380)	28.20	−19.154	296 (20)	0.990
Area ratio	HMB	1.60 (10)	0.1*	0.39 (8)	247240	0.878	−32776 (2930)	26.00	−13.563	272 (24)	0.984
d_{002} spacing	SM	6.992 (17)	6.731 (11)	0.69 (14)	5905	0.957	−40813 (2750)	32.23	−23.546	339 (23)	0.991
FWHM	SM	5.34 (32)	0.42 (16)	0.60 (11)	3358	0.969	−43416 (860)	34.17	−26.050	361(7)	0.999
$L_c(002)$	SM	21.98 (6.4)	163.7 (7.4)	1.09 (26)	33813	0.956	−40198 (1090)	31.54	−21.104	334 (9)	0.999
Area ratio	SM	2.11 (11)	0.1*	0.61 (10)	95374	0.906	−38508 (2110)	30.27	−18.808	320 (18)	0.994

		Fitting data (Power function[a])									
		c	A	b	R^2						
$L_c(002)$	HMB	23.9 (13.6)	2.9	0.31 (6)	0.961		−31312 (1520)	24.70		260 (13)	0.995

[a] $f(t) = A\exp(bt) + c$ [b] $\ln A_1$ is calculated from the intercept of the Arrhenius plot (1/T vs. $\ln t_{half}$)
*Both C_{max} of area ratio is held